Physics of Plasmas

RESEARCH ARTICLE | APRIL 17 2023

Experimental study of the edge radial electric field in different drift configurations and its role in the access to H-mode at ASDEX Upgrade

Special Collection: Papers from the 63rd Annual Meeting of the APS Division of Plasma Physics

U. Plank ; D. Brida ; G. D. Conway ; T. Happel ; A. E. Hubbard ; T. Pütterich ; C. Angioni ; M. Cavedon ; R. Dux ; T. Eich ; R. Fischer; P. Hennequin ; ASDEX Upgrade Team

Phys. Plasmas 30, 042513 (2023)
https://doi.org/10.1063/5.0102763

Physics of Plasmas ARTICLE scitation.org/journal/php

Experimental study of the edge radial electric field in different drift configurations and its role in the access to H-mode at ASDEX Upgrade

Cite as: Phys. Plasmas **30**, 042513 (2023); doi: 10.1063/5.0102763
Submitted: 12 June 2022 · Accepted: 14 March 2023 ·
Published Online: 17 April 2023

U. Plank,[1,a)] D. Brida,[1] G. D. Conway,[1] T. Happel,[1] A. E. Hubbard,[2] T. Pütterich,[1] C. Angioni,[1] M. Cavedon,[3] R. Dux,[1] T. Eich,[1] R. Fischer,[1] P. Hennequin,[4] and ASDEX Upgrade Team[1,b)]

AFFILIATIONS

[1]Max-Planck-Institut für Plasmaphysik, Boltzmannstraße 2, 85748 Garching, Germany
[2]Plasma Science and Fusion Center, MIT, Cambridge, Massachusetts 02129, USA
[3]Dipartimento di Fisica "G. Occhialini," Università di Milano-Bicocca, 20126 Milano, Italy
[4]Laboratoire de Physique des Plasmas, CNRS, Sorbonne Université, Ecole polytechnique, Institut Polytechnique de Paris, 91120 Palaiseau, France

Note: This paper is part of the Special Collection: Papers from the 63rd Annual Meeting of the APS Division of Plasma Physics.
Note: Paper TI2 6, Bull. Am. Phys. Soc. **66** (2021).
[a)]Invited speaker. **Author to whom correspondence should be addressed:** Ulrike.Plank@ipp.mpg.de
[b)]For the ASDEX Upgrade Team, see Stroth *et al.*, Nucl. Fusion **62**, 042006 (2022).

ABSTRACT

The formation of the equilibrium radial electric field (E_r) has been studied experimentally at ASDEX Upgrade (AUG) in L-modes of "favorable" (ion ∇B-drift toward primary X-point) and "unfavorable" (ion ∇B-drift away from primary X-point) drift configurations, in view of its impact on H-mode access, which changes with drift configurations. Edge electron and ion kinetic profiles and impurity velocity and mean-field E_r profiles across the separatrix are investigated, employing new and improved measurement techniques. The experimental results are compared to local neoclassical theory as well as to a simple 1D scrape-off layer (SOL) model. It is found that in L-modes of matched heating power and plasma density, the upstream SOL E_r and the main ion pressure gradient in the plasma edge are the same for either drift configurations, whereas the E_r well in the confined plasma is shallower in unfavorable compared to the favorable drift configuration. The contributions of toroidal and poloidal main ion flows to E_r, which are inferred from local neoclassical theory and the experiment, cannot account for these observed differences. Furthermore, it is found that in the L-mode, the intrinsic toroidal edge rotation decreases with increasing collisionality and it is co-current in the banana-plateau regime for all different drift configurations at AUG. This gives rise to a possible interaction of parallel Pfirsch–Schlüter flows in the SOL with the confined plasma. Thus, the different H-mode power threshold for the two drift configurations cannot be explained in the same way at AUG as suggested by LaBombard *et al.* [Phys. Plasmas **12**, 056111 (2005)] for Alcator C-Mod. Finally, comparisons of E_r profiles in favorable and unfavorable drift configurations at the respective confinement transitions show that also the E_r gradients are all different, which indirectly indicates a different type or strength of the characteristic edge turbulence in the two drift configurations.

I. INTRODUCTION

The underlying mechanism for the transition from L- to H-mode confinement (L-H transition) has been of interest since the discovery of the H-mode on the ASDEX tokamak.[2] The equilibrium radial electric field, E_r, at the plasma edge is often considered to be responsible for the transition into the H-mode, as its gradients are connected to a background $E \times B$ shear flow, which can stabilize the underlying edge turbulence.[3] The condition for the H-mode access is then that the shearing rate of the $E \times B$ velocity ($v_{E\times B}$) is large enough to suppress the characteristic turbulence at the plasma edge. At ASDEX Upgrade

(AUG), it has been found in experiments in the standard configuration (lower single-null favorable drift configuration) that the minimum of $v_{E\times B}$, which is a proxy for its shear in these conditions, is constant at the L-H transition for a wide range of densities, magnetic field strengths, and different isotopes (D and H).[4] This finding not only indicates that $v_{E\times B}$ and its connected shear play a crucial role for the confinement transition but also indirectly suggests that the underlying edge turbulence may be unchanged for this parameter range.

On a macroscopic scale, the transition into the H-mode occurs if sufficient auxiliary heating power is applied. The so-called H-mode power threshold (P_{LH}) exhibits many dependencies that are not always consistent between the different tokamaks.[5] However, one robust observation that has been made on several devices is that P_{LH} changes by more than a factor of two if either the toroidal magnetic field is reversed or if the configuration is switched from lower single-null (LSN) to upper single-null (USN).[2,6–9] A magnetic configuration in which the ∇B-drift of the main ions ($v_{\nabla B,i}$) points toward the primary X-point exhibits a lower P_{LH} than one in which $v_{\nabla B,i}$ points away from the primary X-point. For this reason, the first one is termed "favorable" drift configuration, whereas the latter is referred to as "unfavorable" drift configuration.

As of yet, it has not been clarified unambiguously why P_{LH} alters with drift configuration, but it is considered that it is connected to changes in the local edge parameters and the resulting edge turbulence. Previous experimental observations on several tokamaks, including DIII-D, AUG, and WEST, have consistently shown that E_r in the confined plasma edge region is different between the two drift configurations.[10–12] The resulting differences in the E_r gradients could directly influence the criterion of turbulence suppression by $E\times B$ mean shear flows. Divertor profile measurements together with scrape-off layer (SOL) modeling results also show changes of the upstream E_r in the SOL with the switch of the drift configuration.[13,14] Modifications in the SOL E_r could also impact the strength of the $E\times B$ shear flows and, as such, lead to differences in the H-mode onset between the two drift configurations. At Alcator C-Mod, it was observed that the SOL flows change with the drift direction and that they possibly set a boundary condition for the intrinsic toroidal edge rotation v_ϕ, which, in turn, influences E_r (Ref. 1). In the study of Alcator C-Mod, the L-H transition occurred in both drift configurations if v_ϕ was of the same size and co-current, leading to a threshold behavior in $v_{E\times B}$ at the L-H transition, which could then be related to the increased P_{LH} in the unfavorable drift configuration. Another possible mechanism recently discussed is connected to a change in the characteristic edge turbulence with the reversed ∇B-drift direction, which would also lead to the existence of the I-mode in the unfavorable drift configuration.[15] It is conceivable that such a change in the edge turbulence leads to modified requirements for the $E\times B$ shear flow needed to suppress the characteristic edge turbulence, resulting in a higher P_{LH} in the unfavorable drift configuration. Other theories deal with the differences in the parallel momentum transport due to the up-down asymmetry of the magnetic geometry, which could impact both the edge turbulence and the mean-field E_r simultaneously, but differently for the two drift configurations.[16,17] Also ion orbit losses close to the boundary of the confined plasma[18] or the interaction with neutrals penetrating into the confined plasma—both mechanisms have been found to depend on the exact magnetic configuration[19–21]—have been considered as possible candidates for the observed differences in E_r and the altered H-mode power threshold in the two drift configurations since long.

In view of possible explanations for the altered H-mode access conditions between the different drift configurations, the experimental work presented here focuses on the characterization of the equilibrium edge radial electric field and related quantities, like the main ion pressure gradient and the edge rotation, in the L-mode and at the L-H transition in the two different drift configurations. Thanks to new and improved diagnostic techniques, special emphasis can be put on the analysis of the E_r gradient across the separatrix, which connects the confined plasma and SOL. The measurements are compared with predictions of local neoclassical theory in the confined plasma and with a simple 1D model for the upstream E_r in the SOL. Based on these results, it is discussed whether the theories introduced above could be valid candidates to explain the increased P_{LH} in the unfavorable drift configuration. Furthermore, the current observations are brought in context with previous experimental findings in order to identify key mechanisms important for the L-H transition in general, which then can serve for validation of theoretical models aiming to predict the L-H transition self-consistently.

The paper is organized as follows: Sec. II reviews the properties of the edge and SOL E_r. Section III introduces the design of the experiments and the analysis methods. Section IV compares the H-mode power threshold in the different drift configurations, and Sec. V describes the corresponding evolution of the outer E_r gradient during the transition from the L- to H-mode. Section VI compares edge and outer divertor target profiles in L-modes of different drift configurations at matched density and heating power. Section VII presents results on the behavior of E_r in the L-mode with changing density and heating power. Section VIII compares E_r profiles at the confinement transition in favorable and unfavorable drift configurations. Section IX summarizes the results from this experimental study and discusses the conclusions drawn from them.

II. PROPERTIES OF E_r FROM THE PLASMA EDGE TO THE SCRAPE-OFF LAYER

The radial electric field E_r can be determined starting with the momentum balance equation for a plasma species α:

$$m_\alpha n_\alpha \frac{\mathrm{d}\boldsymbol{u}_\alpha}{\mathrm{d}t} = q_\alpha n_\alpha(\boldsymbol{E}+\boldsymbol{u}_\alpha\times\boldsymbol{B}) - \nabla p_\alpha - \nabla\boldsymbol{\Pi}_\alpha + \boldsymbol{R}_\alpha. \quad (1)$$

Here, m_α is the mass, n_α is the number density, $\boldsymbol{u}_\alpha$ is the fluid velocity, q_α is the charge, and p_α is the scalar pressure of α. $\boldsymbol{\Pi}_\alpha$ is the viscous stress tensor and $\boldsymbol{R}_\alpha$ is the friction force between species α and all other plasma species. $\boldsymbol{E}$ and $\boldsymbol{B}$ are the local electric and magnetic field, respectively.

Under stationary conditions, i.e., $m_\alpha n_\alpha \mathrm{d}\boldsymbol{u}_\alpha/\mathrm{d}t = 0$, and if friction forces are neglected, Eq. (1) simplifies in the first order of the Larmor radius $r_{\mathrm{L},\alpha}$ to[22]

$$\nabla p_\alpha = q_\alpha n_\alpha(\boldsymbol{E}+\boldsymbol{u}_\alpha\times\boldsymbol{B}). \quad (2)$$

This equation has to be fulfilled by each single plasma species α, but in the following, we concentrate on the relation of E_r with the properties of the main ion (i) and electron (e) species.

In the confined plasma, E_r is determined by the main ion quantities and Eq. (2) can be re-written as the well-known radial force balance equation,

$$E_r = \frac{\nabla_r p_i}{Z_i e n_i} + v_i \times B = \frac{\nabla_r p_i}{Z_i e n_i} - v_{\theta,i} B_\phi + v_{\phi,i} B_\theta, \tag{3}$$

where $\nabla_r \equiv \partial/\partial R$, Z_i is the charge number, $v_{\theta,i}$ is the poloidal and, $v_{\phi,i}$ is the toroidal velocity of the main ion species i, and B_ϕ and B_θ are the toroidal and poloidal field components, respectively. Please note that we assume a right-handed (R, Θ, Φ) system, which is in accordance with the coordinate system of AUG. Further details on AUG's coordinate system and the sign conventions can be found in Appendix A. In addition to this, in the present work, v_ϕ is positive if it is in the same direction as I_p (i.e., co-current), unless it is stated differently.

In the H-mode, it is often observed that $v_i \times B$ is small[23,24] and, thus,

$$E_r \approx \frac{\nabla_r p_i}{Z_i e n_i} < 0. \tag{4}$$

In the SOL, an expression for the electric field parallel to the magnetic field lines $E_\parallel$ can be derived from Eq. (1),[25]

$$E_\parallel = \frac{j_\parallel}{\sigma_\parallel} - \frac{1}{e n_e} \nabla_\parallel p_e - \frac{0.71}{e} \nabla_\parallel T_e. \tag{5}$$

Here, $j_\parallel$ is the parallel current density and $\sigma_\parallel$ is the parallel electrical conductivity. n_e, p_e, and T_e are the electron density, pressure, and temperature, respectively. This parallel force balance equation is also known as Ohm's law of the SOL since it connects the electric field with the current density.[26]

The electric potential V_{pl} at the outer midplane (OMP) can be obtained by integrating Eq. (5) in the SOL from the outer divertor target plate (denoted with "t") upstream to the OMP. For an analytic solution, the following assumptions are made: $j_\parallel/\sigma_\parallel$ is neglected, since it is found to be small, at least in LSN favorable drift configuration L-modes,[27,28] and $p_e = p_{e,t}(\frac{T_e}{T_{e,t}})^a$ is assumed.[29] This gives the following expression for V_{pl}:

$$V_{pl} = \frac{2.8}{e} T_{e,t} + V_{fl} + \frac{0.71 + a}{e} (T_{e,OMP} - T_{e,t}), \tag{6}$$

where V_{fl} is the potential of the electrically floating divertor target plates and $a = \frac{0.47}{\log(T_{e,OMP}/T_{e,t})}$ at AUG.[27] E_r in the SOL at the OMP is then calculated as

$$E_r = -\nabla_r V_{pl}. \tag{7}$$

In the conduction-limited regime, $T_{e,OMP} \gg T_{e,t}$. If also V_{fl} is small, Eq. (6) simplifies with Eq. (7) to[26]

$$E_r \approx -\frac{1}{e} \nabla_r T_{e,OMP} > 0. \tag{8}$$

Combining Eqs. (4) and (8) shows that E_r changes sign close to or at the separatrix (i.e., at the normalized poloidal magnetic flux $\rho_{pol} = 1$). From this, the following structure of E_r is expected in the plasma edge and SOL (see also Fig. 2): In the confined region, E_r exhibits a negative well, with its minimum ($E_{r,min}$) located near, but inside the separatrix. In the SOL, E_r has a hill structure, with $E_{r,max}$, the maximum of the hill, and a decay toward the far SOL. The negative E_r gradient, entirely located in the confined region, is termed the "inner" E_r gradient in the following. In contrast, the "outer" E_r gradient is the positive one at the separatrix, which connects $E_{r,min}$ and $E_{r,max}$. In the paradigm of the critical $E \times B$ shear needed to suppress the edge turbulence at the L-H transition, it has not been identified yet, whether both E_r gradients are responsible for the L-H transition or if either the inner or the outer E_r gradient is the important one. At AUG, recent experimental observations indicate that the turbulence suppression starts at the location of the inner E_r gradient.[30]

III. METHODOLOGY

In the following, the design of the experiments and the different analysis methods are introduced.

A. Discharge design

Figure 1 shows a typical L-H transition plasma discharge at AUG (the reference discharge, #35842). It is in LSN favorable drift configuration, with a toroidal magnetic field of $B_\phi = -2.5$ T at the geometric axis, a plasma current of $I_p = +800$ kA, and a safety factor of $q_{95} = -5$ (see also Appendix A for the sign conventions of AUG). Several versions of this reference discharge were performed and analyzed, with modifications of different parameters (plasma density, drift configuration, and heating method).

For most of the L-H transition discharges, electron cyclotron resonance heating (ECRH) power ramps were applied to trigger the transition into the H-mode [see Fig. 1(a)]. For this type of heating scheme, the label "ECRH" is used in the following. X2 mode heating at

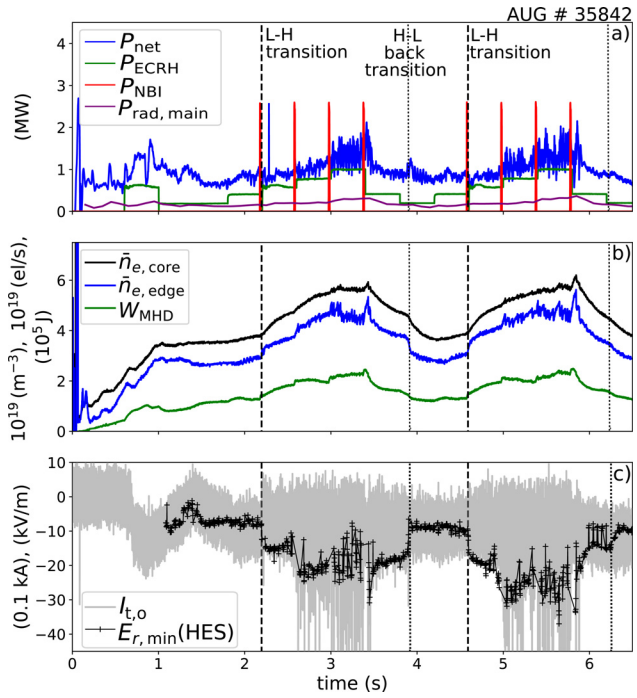

FIG. 1. Reference L-H transition discharge in the LSN favorable drift configuration. Time traces of (a) auxiliary heating power (green, red), the net input power (blue), and main chamber radiation (purple). Time evolution of (b) the line-averaged electron density at the plasma core (black) and edge (blue) and of the stored thermal energy (green). (c) Evolution of the minimum of E_r (black) and the signal of the outer shunt current measurement (gray), which can be used as indicators of the L-H and H-L back transitions. The L-H transitions and the H-L back transitions of this discharge are marked by the vertical dashed and dotted lines, respectively.

140 GHz was employed, which deposits the heating power near the magnetic axis. The power was stepwise increased by 200–300 kW to pinpoint P_{LH}. Each power step was chosen to be at least 150 ms long to reach steady-state conditions (the confinement time τ_E = 100–140 ms in the investigated L-mode conditions). During each heating step, a slow strike-point sweep (covering approximately 2 cm in about 100 ms) along the outer divertor target was accommodated for a better coverage of Langmuir probe (LP) measurements. At the end of each heating step, a 10 ms long blip of the neutral beam injection (NBI) with a nominal power of 2.5 MW per blip was applied for charge exchange recombination spectroscopy (CXRS) measurements on fully stripped low-Z impurities (boron and nitrogen). Each NBI blip is a small perturbation to the plasma and increases the net input power [P_{net}, see Eq. (9)] by about 200 kW for approximately 50 ms. This amount of heating is within the uncertainties of the P_{LH} determination, but it was regularly observed that the additional power of the NBI blip triggered the L-H transition. However, the H-mode could then only be sustained if after the perturbation by the NBI blip sufficient additional ECRH was applied. Otherwise the plasma transited back into the L-mode after the perturbation by the NBI blip. Furthermore, if no NBI blips were applied, then the plasma entered H-mode in the subsequent ECRH step, which confirms the assumption that the additional power introduced by the NBI blip is of the same size as the ECRH power steps.

In a few L-H transition experiments, also dominant ion heating was applied. For these discharges, the NBI was modulated and the frequency of the modulation was stepwise increased such that effectively heating power steps of 200–300 kW were achieved.[31] For this heating scheme, also a small amount of central ECRH (200–300 kW) was applied continuously. It is referred to this heating scheme as "NBI+ECRH" in the following.

Figure 1(b) shows the time traces of the core and edge line-averaged densities of the deuterium cyanide laser interferometer ($\bar{n}_{e,core}$ and $\bar{n}_{e,edge}$) (Ref. 32), which correspond to approximate ρ_{pol} positions of 0.4 and 0.95, respectively. The target density for the reference discharge was chosen to be $\bar{n}_e \approx 4.5 \times 10^{19} m^{-3}$, as it is the density for which the L-H transition occurs at the lowest heating power in deuterium (D) plasmas in standard drift configuration at AUG ($\bar{n}_{e,min}$) (Ref. 33). To achieve this density, a D fueling rate of about 3×10^{21} el/s from the divertor was needed. In USN discharges, where the pumping efficiency is lower due to the lack of a cryostatic pump in the upper divertor, substantially lower fueling rates are needed to get this desired density. Also, if the intrinsic B concentration was too low for CXRS measurements, small amounts of N were injected. The low-Z impurity content was monitored with the CXRS diagnostics[34] and found to be below 1%, leading to an average Z_{eff} of about 1.2–1.4 (Ref. 35).

Starting from the reference discharge, several modifications were applied to it and the impact on the L-H transition power, on the density, temperature, and E_r profiles at the OMP and at the outer divertor target in the vicinity of the separatrix was studied. The plasma density and the heating mix (ECRH and NBI) were altered for both favorable and unfavorable drift configurations. Pairs of L-H transition discharges in forward and reversed magnetic field direction were performed in both LSN and USN configurations. In this way, also a possible impact of the different divertor geometries (closed divertor in LSN and open divertor in USN) on P_{LH} could be addressed for either drift configuration. The exact magnetic geometries with their respective drift directions and how they can be achieved at AUG are described in more detail in Appendix A.

In the upcoming plots, shades of the color blue are used for plasmas in the LSN favorable drift configuration, purple for the USN favorable drift configuration, red for the LSN unfavorable drift configuration, and orange for the USN unfavorable drift configuration.

B. Determination of the L-H transition time and power

The L-H transition time point (t_{LH}) was determined using several different diagnostic signals. One important feature of the L-H transition is the sudden increase in the edge density and the stored thermal plasma energy W_{MHD} [see Fig. 1(b)]. Further measurements employed to pinpoint t_{LH} are the shunt current measurements of the inner and outer target tiles, $I_{t,i}$ and $I_{t,o}$, and poloidal magnetic field fluctuation ($\dot{B}_\theta$) measurements of two Mirnov coils located close to the primary and secondary X-points. Also the minimum of the edge radial electric field, here determined with He II spectroscopy (HES)[36] (see Sec. III E), shows a sudden drop at the L-H transition and is, therefore, a useful indicator of the L-H transition [see Fig. 1(c)]. A more detailed description on the use of these different diagnostics to determine t_{LH} can be found in previous AUG-related publications on the L-H transition.[4,31] Taking into account the information of these different signals allows for a determination of t_{LH} with high precision (±1 ms uncertainty).

In the favorable drift configuration, the plasma enters a dithering phase at t_{LH}, which is termed I-phase at AUG[37–39] and found also at other machines.[40–42] It is regularly observed that the plasma develops from the I-phase, which exhibits periodic oscillations, into a rather bursty state, which is often identified as a type-III ELMy H-mode, before the type-I ELMy H-mode is observed. Concomitant with this development, a continuous increase in plasma confinement is observed. The I-phase oscillations have a frequency of a few kHz[43] and can be seen as a modulation on $I_{t,i}$ and $I_{t,a}$, and also on $\dot{B}_\theta$. Therefore, these signals are a precise indicator of t_{LH}.

The I-phase should not be confused with the I-mode. The latter is, in addition to the L- and H-modes, another confinement regime, which is normally observed in unfavorable drift configuration.[6,9,44] The I-mode exhibits improved energy, but L-mode-like particle confinement[6,9,44,45] and can be operated as a stable regime.[9,46] The I-mode occurs and evolves, in terms of heating power, between L-mode and H-mode (see also Fig. 5). Therefore, in the unfavorable drift configuration, the L- to H-mode transition can be separated into a transition from the L- to I-mode (L-I transition) at t_{LI} and a transition from the I- to H-mode (I-H transition) at t_{IH}. For the determination of t_{LI} and t_{IH}, the same diagnostics as described above for the determination of t_{LH} are used. Additional information is taken from edge temperature and reflectometer (density fluctuation) measurements, as the I-mode is characterized by a pedestal structure in T_i and T_e and the existence of a weakly coherent mode (WCM) at approximately 100 kHz, located at the plasma edge.[9] In the I-mode, no or only a weak increase in the edge plasma density is observed,[47] while a sharp increase in the plasma density occurs only at the H-mode onset at t_{IH}.

The definitions of t_{LH}, t_{LI}, and t_{IH} here are consistent with the ones used in previous L-H transition and I-mode studies at AUG.[4,46] If not stated differently, the edge electron density and temperature profiles (which are referred to as "kinetic" in the following), and the E_r profiles, which are shown in this article, are taken from stable L-mode or I-mode phases. For this, the profiles were averaged over time

windows of 50–150 ms duration. The time windows in the stable phases extend until at most 15 ms before the defined L-H, L-I or I-H transition time. The ion temperature and impurity rotation profiles are taken from the NBI blip closest to this time window, averaged over the entire length of the NBI blip.

The H-mode power threshold P_{LH} in favorable drift configuration (I- and H-mode power thresholds P_{LI} and P_{IH} in the unfavorable drift configuration) is defined as the net input power P_{net} at t_{LH} (t_{LI} and t_{IH}), where

$$P_{net} = P_{heat} - \frac{dW_{MHD}}{dt} = P_{OH} + P_{aux} - \frac{dW_{MHD}}{dt}. \quad (9)$$

P_{heat} is hereby the absorbed heating power from all heating contributions, namely, the Ohmic power P_{OH} introduced through the plasma current and all auxiliary heating contributions $P_{aux} = P_{NBI} + P_{ECRH}$, corrected for their respective losses.[31,48,49] P_{net} also includes a correction for changes of the plasma stored energy dW_{MHD}/dt. The main chamber radiation $P_{rad,main}$, reconstructed from bolometer measurements,[50] is not taken into account in the calculation of P_{net}, since it has been found to show little variation at the L-H transition between the different discharges, and it is also small, between 300 and 500 kW, for all investigated discharges. Time traces of P_{net}, P_{ECRH}, P_{NBI}, and $P_{rad,main}$ are depicted for the reference discharge in Fig. 1(a).

C. Power balance analysis

The power balance analysis was performed in order to deduce the surface-integrated edge ion and electron heat fluxes ($Q_{i,edge}$ and $Q_{e,edge}$) at the L-H transition. For this, the transport code ASTRA was employed in an interpretive mode.[51] To determine the exact heat deposition profile of the ECRH, the microwave beam tracing code TORBEAM[52] was used and for the NBI deposition profile, the real-time code RABBIT[49] was coupled to ASTRA.

Consistent with previous L-H transition studies at AUG,[31,48] the total edge ion and electron heat fluxes were evaluated at the radial position of $\rho_{pol} \approx 0.98$, where ρ_{pol} is the normalized poloidal magnetic flux.

D. Edge kinetic profile measurements and alignment

For an exact reconstruction of the magnetic equilibrium in all investigated magnetic configurations, the Grad–Shafranov equation is coupled with the current-diffusion equation.[53] Furthermore, other constraints on the equilibrium, e.g., the measurements of the thermal pressure profile, are taken into account in the framework of Bayesian probability theory.[32,53] This leads to an uncertainty of about 1 cm for the separatrix position in the L-mode at the outer midplane, which corresponds to $\Delta\rho_{pol} \approx 0.014$ for the here investigated plasma shapes.[54]

The T_e and n_e profiles presented in this work were determined using an integrated data analysis (IDA) of several diagnostics.[32] The T_e profiles were shifted radially in such a way that the prediction for $T_{e,sep}$, employing Spitzer–Härm power balancing,[55–57] was fulfilled. The radial shifts of the n_e profiles were determined from the radial shifts of the Thomson scattering and the He I beam data,[58] which measure T_e and n_e at the same location simultaneously. The impurity temperature (T_{imp}) and the toroidal and poloidal velocity ($v_{\phi,imp}$ and $v_{\theta,imp}$) profiles, which were determined with CXRS,[59,60] were not shifted radially. Furthermore, in this study, it is assumed that the main ion temperature T_i equals the temperature of the impurity ions T_{imp}, which is a valid assumption in AUG H-modes,[61] but has been found to be incorrect at other machines like DIII-D.[24] For the uncertainty estimation of the main ion pressure gradient profiles $[(\nabla_r p_i)/(en_i)]$, a relative shift of the T_i profiles of ±5 mm with respect to the validated n_e profiles was applied.

E. E_r profile measurements and alignment

The edge E_r profiles at the OMP were determined using Doppler V- and W-band reflectometry in X-mode (DR)[62,63] and He II spectroscopy (HES).[36] The latter relies on the Doppler spectroscopy of singly ionized helium.[64] Thermal He is periodically injected by a piezoelectric gas valve with on-off times of about 50 ms. The neutral He particles get ionized and excited by plasma interactions (mainly electron impact ionization and excitation), and the emitted light is detected by a spectroscopic system. From the width of the characteristic spectral line, the local He^{1+} temperature, from its Doppler shift, the He^{1+} flow speed, and from its intensity, the local He^{1+} density can be determined.[36] In this way, this technique allows for a local measurement of E_r employing the radial force balance equation [see Eq. (3)] for the singly ionized He particles instead of for the main ions.[36] It turns out that this E_r measurement technique is restricted to a region of ρ_{pol} 0.98 to approximately 1.02, i.e., the region of the outer E_r gradient, whereas the inner E_r gradient cannot be resolved by HES. Furthermore, the spectroscopic system has an acquisition time of $\Delta t_{acquisition} = 2.45$ ms, which makes this E_r measurement technique not suitable to detect transient phenomena or events, which are faster than this timescale, e.g., a resolved measurement of the I-phase oscillations.

For the localization of the DR-E_r data, the validated n_e profiles (see Sec. III D) were used. A detailed comparison between the DR and HES diagnostics and a forward model developed for the HES method showed excellent agreement between the two E_r measurements in all four investigated drift configurations.[36] The determined E_r profiles across the separatrix agree in both size and shape of the outer E_r gradient and its radial position. From these comparisons, it was also concluded that the turbulence phase velocity, which would be detected by DR, but not by HES, must be small (no larger than a few hundreds of m/s) in the plasma edge in the L-mode.

An example measurement of the three different edge E_r diagnostics is shown for the reference discharge #35842 in Fig. 2. Here and in the following radial profiles are plotted against ρ_{pol}. Since the agreement between the different E_r diagnostics is excellent (below 1 kV/m deviation), normally only one E_r profile is shown in the course of this article. However, a comparison between the different diagnostics has always been performed, if measurements from them were available. In the following, these symbols are used (see also Fig. 2): Stars denote E_r measurements from the V-band DR, squares from the W-band DR, and circles from HES.

The $E_{r,min}$ and $E_{r,max}$ values were determined as the minimal and maximal measured values of E_r in the radial region $\rho_{pol} \approx 0.98$–1 and $\rho_{pol} \approx 0.995$–1.02, respectively.

F. Neoclassical calculations

For the deduction of the poloidal and toroidal main ion flows, and with Eq. (3) also of the edge radial electric field, local neoclassical (NC) theory was employed. The NC calculations were performed with

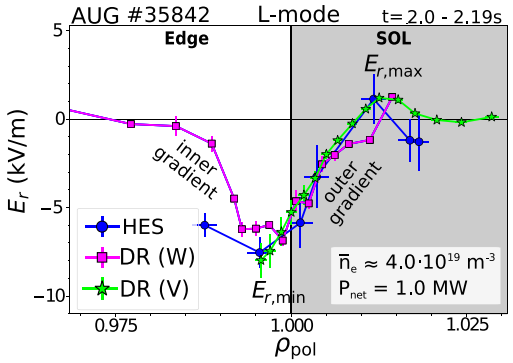

FIG. 2. Comparison of measured edge E_r profiles. E_r profiles detected with V- and W-band Doppler reflectometry (DR, stars and squares) and He II spectroscopy (HES, circles) in a stable L-mode phase of the reference discharge (see Fig. 1). The profiles are plotted against the normalized poloidal flux coordinate ρ_{pol}, where $\rho_{pol} = 1$ denotes the separatrix. The negative E_r gradient located entirely in the confined plasma is termed "inner" E_r gradient, whereas the positive E_r gradient connecting $E_{r,min}$ and $E_{r,max}$ is termed "outer" E_r gradient.

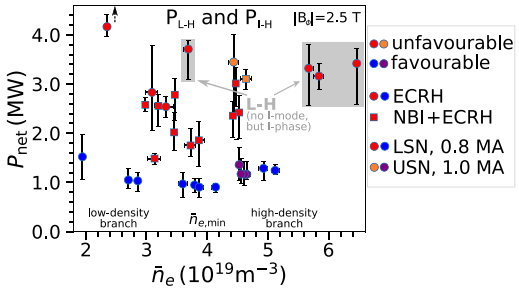

FIG. 3. Density dependence of the H-mode power threshold in favorable and unfavorable drift configuration. Net input power at the L-H transition (P_{LH}, blue and purple) and I-H transition (P_{IH}, red and orange) vs line-averaged core electron density, $\bar{n}_e$. Circles denote dominant ECRH heating, whereas squares denote a mixture of NBI and ECRH heating. The arrow at the data point in unfavorable drift configuration at low density indicates that this is a lower boundary for P_{IH}. Also, for the favorable drift configuration plasmas, the region of the density minimum and the low and high density branches of P_{LH} are denoted.

the code NEOART,[65] which was bench-marked against the NEO code[66] for a subset of discharges in the different drift configurations. For a given impurity, NEOART solves the set of linear coupled equations of the parallel velocity in all collision regimes for each charge state.[67] NEOART includes the collisions of the considered impurity ion with the main plasma ions i and all other impurities. The experimentally determined radial profiles of the electron density and temperature (n_e and T_e), the main ion temperature (T_i), and the density and toroidal rotation of the impurity (n_{imp} and $v_{\phi,imp}$) are given as input to the code, which calculates the NC poloidal main ion and impurity velocity profiles ($v_{\theta,i}$ and $v_{\theta,imp}$) and the differential of the toroidal main ion rotation ($v_{\phi,i}$) to a given $v_{\phi,imp}$.

In all the NEOART calculations, it was assumed that besides the main ion species (D), only one impurity species is present in the plasma edge (B or N). If possible, the corresponding impurity density n_{imp} was deduced from the radiance of the CXRS measurements.[34] To calculate the main ion density, n_i, the charge state distribution of the investigated impurity has to be known. This was determined assuming the coronal ionization equilibrium. Since the actual impurity density at the plasma edge could not always be determined experimentally, two different assumptions were made and the resulting n_i profiles compared. For the first one, it was assumed that the impurity density is the one of the fully ionized impurity, e.g., $n_N = n_{N^{7+}}$. For the second approach, a constant impurity concentration of 1% was assumed over the investigated radial range, i.e., $n_{imp} = 0.01\, n_e$. It was found that the resulting n_i profile does not differ strongly, using the two different assumptions on n_{imp}. Therefore, if no n_{imp} measurements were available, a constant impurity concentration of 1% was assumed, which is in good agreement with the experimentally determined Z_{eff} values from Bremsstrahlung measurements.[35]

IV. H-MODE POWER THRESHOLD IN DIFFERENT DRIFT CONFIGURATIONS

Figure 3 shows the net input power P_{net} at the L-H transition (P_{LH}, blue and purple) in the favorable drift configuration (LSN and USN) and at the I-H transition (P_{IH}, red and orange) in the unfavorable drift configuration (LSN and USN), plotted against the line-averaged electron density $\bar{n}_e = \bar{n}_{e,core}$. In all plotted discharges, $|B_\phi| = 2.5$ T at the geometric axis, whereas $|I_p| = 0.8$ MA for the LSN and $|I_p| = 1$ MA for the USN discharges. The values of the power threshold agree within one drift configuration, regardless whether LSN or USN plasmas are investigated, which indicates that the exact divertor configuration (open vs closed divertor, see also Appendix A for the divertor geometry) has minor impact on the power threshold in these discharges. Furthermore, there is no difference seen in the H-mode power threshold between the 0.8MA and the 1MA datasets, which is in agreement with previous observations at AUG of favorable drift configuration plasmas, where for plasmas located in the high-density branch, no dependence of P_{LH} on I_p is found.[68]

As observed at several tokamaks, P_{IH} in the unfavorable drift configuration is 2–3 times higher than P_{LH} in the favorable drift configuration.[9,69,70] For P_{LH}, the typical parabolic dependency on $\bar{n}_e$ is found, with $\bar{n}_{e,min} \approx 4.0 \times 10^{19}$m^{-3}, the commonly observed value of the density minimum at AUG in the favorable drift configuration.[48,68] However, P_{IH} does not show such a parabolic dependence on $\bar{n}_e$, instead it exhibits a large scatter for a fixed $\bar{n}_e$. This behavior of P_{IH} has already been mentioned in previous work from AUG,[69] where it was pointed out that it might be connected to the exact development of the preceding I-mode. Another reason for the larger scatter in P_{IH} could be connected to the fact that the unfavorable drift configuration data are from pure ECRH and mixed NBI+ECRH heated plasmas. From L-H transition studies in the favorable drift configuration, it is known that P_{LH} depends on the employed heating method in the low-density branch. This observation is connected to a critical $Q_{i,edge}$ needed to enter the H-mode and the different efficiency of ECRH and NBI to heat the ions[31,48] as well as the impact of external torque input on P_{LH} (Refs. 48 and 71), which occurs with NBI, but not with ECRH.

Since power balance calculations could not be performed for all of the discharges under study, mostly, due to a lack of full-radius T_i profiles, it cannot be confirmed whether $Q_{i,edge}$ is the same at the I-H confinement transition for discharges with either heating mix. It appears, however, that the discharges with NBI have a lower P_{IH} than their counterparts with ECRH only, which indicates that $Q_{i,edge}$ could also be an important quantity at the I-H confinement transition.

Furthermore, there is one data point at low density in Fig. 3, marked with an upward facing arrow, which would confirm the critical role of $Q_{i,\mathrm{edge}}$ for the H-mode transition physics also in the unfavorable drift configuration. The given value of P_{IH} for this discharge (AUG #37375) is only a lower boundary, since the plasma neither transited into I- nor H-mode. Power balance calculations for this data point give $Q_{i,\mathrm{edge}} \approx 0.59$ MW, which is below the critical $Q_{i,\mathrm{edge}}$ of about 0.71 MW needed to transit from the L- into I-mode in these plasma conditions at AUG.[69]

Another interesting observation is that some of the discharges in unfavorable drift configuration did not enter the I-mode before transiting into the H-mode, but a direct transition from the L- to H-mode occurred, with the typical signatures of an I-phase during the transition. As stated in Sec. III B, the I-phase is always observed in the favorable drift configuration at the L- to H-mode transition. In Fig. 3, the unfavorable drift configuration cases with a direct L-H transition are highlighted in gray. As of yet, it is not clear which conditions or parameters determine whether an I-mode or an I-phase occurs in the transition from L- to H-mode in the unfavorable drift configuration; however, the two regimes have not yet been observed to appear simultaneously. Figure 3 suggests that I-phases in unfavorable drift configuration plasmas tend to appear at higher densities.

V. EVOLUTION OF E_r IN THE TRANSITION FROM L- TO H-MODE

A. Favorable drift configuration

Figure 4 shows the time evolution of global and edge plasma quantities in a LSN discharge in favorable drift configuration (AUG #36983), transiting from L-mode (light blue) to H-mode (dark blue) via I-phase (blue). The presented discharge was density feedback controlled to $\bar{n}_e \approx 3 \times 10^{19}\mathrm{m}^{-3}$. Except for this lower density, the design of the discharge was as for the reference discharge #35842, introduced in Sec. III. For such discharges, namely, ECRH discharges located on the low-density branch of P_{LH} (see Fig. 3), it is regularly observed that the confinement improvement at or directly after the L-H transition is not as pronounced as for the same type of L-H discharges at higher density, at least for the same plasma current [compare also Figs. 1(b) and 4(b)]. For example, in this low density discharge, no pure type-I ELMy H-mode was observed, although the auxiliary heating power was increased to 3.5 MW. However, the development of $(\nabla_r p_i)/(en_i)$ and E_r during the L-H transition, as shown in Fig. 4(d), are found to be the same for all investigated discharges in favorable drift configuration (in both LSN and USN plasmas), independent of the plasma density and type of applied auxiliary heating.

The E_r profiles across the separatrix [Fig. 4(d)] as well as the time evolution of the E_r minimum [Fig. 4(c)] were measured with the HES diagnostic (see Sec. III E). Each E_r profile is averaged over the acquisition time of 2.45 ms; thus, these are measurements of the mean-field E_r structure. It should be noted that the HES measurements are such that during each He gas puff of about 50 ms length, several profiles are acquired [see also the time trace of $E_{r,\mathrm{min}}$ in Fig. 4(c)]. Therefore, the development of the E_r profile during the L-H transition does not look continuous in Fig. 4(d), which can, however, be attributed to the timing of the He gas modulation with respect to the L-H transition. The analysis of several L-H transitions has shown that the development of E_r, i.e., the steepening of the E_r gradients, is rather continuous during the L-H transition. Figure 4(d) also depicts $(\nabla_r p_i)/(en_i)$ at the plasma edge for the different confinement regimes, which was reconstructed from the experimental edge T_i and n_e profiles, assuming $n_i = n_e$.

The L-H transition is triggered by the NBI blip, at 2.78 s, at a power of about $P_{\mathrm{LH}} = 1.1$ MW. As can be seen in Fig. 4(b) in the time traces of plasma density and stored energy (blue and green), the confinement improvement at the L-H transition is weak. Although $T_{e,\mathrm{edge}}$,

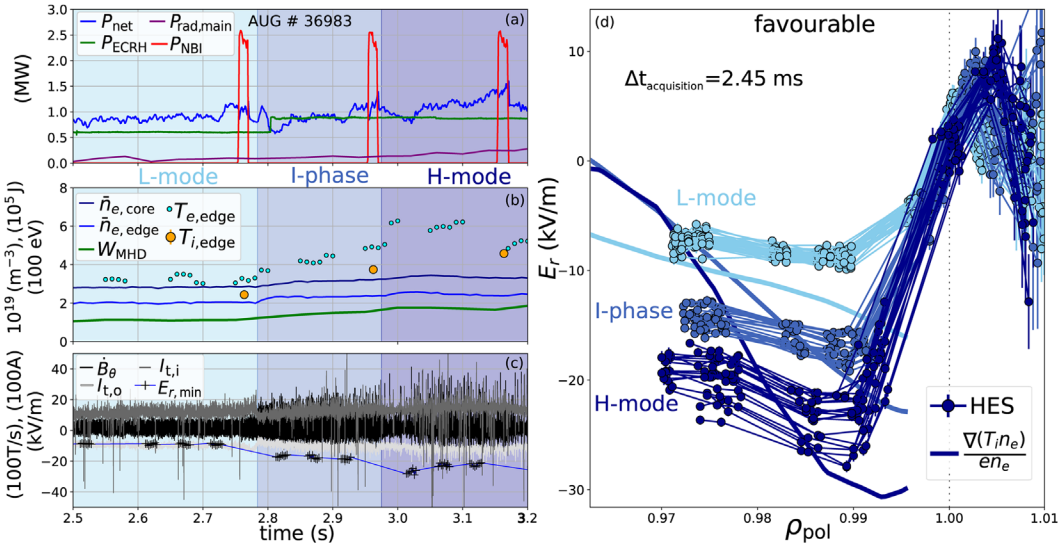

FIG. 4. Evolution of the L-H transition in the favorable drift configuration. Time traces of (a) NBI and ECRH power (red, green), net input power (blue), and main chamber radiation (purple) during an L-H transition. Corresponding evolution of (b) line-averaged electron density in the plasma core and edge (dark blue, blue), stored plasma energy (green), edge electron and ion temperature (cyan and orange), and (c) magnetic field fluctuations (black), inner and outer shunt current signals (silver and gray) and the minimum of the edge radial electric field (blue). (d) Evolution of the outer E_r gradient and $(\nabla_r p_i)/(en_i)$ at the plasma edge during the L-H transition.

measured at $\rho_{pol} = 0.98$, exhibits some variation, the overall trend is that $T_{e,edge}$ (cyan) and $T_{i,edge}$ (orange) increase from L- to I-phase to H-mode, which is also confirmed by the steepening of $(\nabla_r p_i)/(en_i)$ [see Fig. 4(d)]. The analysis of several L-H transition discharges has shown that $(\nabla_r p_i)/(en_i)$ steepens mainly due to a steepening of the T_i gradient, whereas the logarithmic edge density gradient is rather constant in the different confinement regimes.[36,72]

The evolution of the edge E_r from L- to H-mode follows to first order the evolution of $(\nabla_r p_i)/(en_i)$. However, in the L-mode, systematic deviations between $(\nabla_r p_i)/(en_i)$ and E_r are observed, which indicates that the contribution from the plasma flows ($v_i \times B$) to E_r is non-negligible in the L-mode. This is discussed in more detail in Sec. VI. Furthermore, the measurements show that during the entire L-mode phase, the outer E_r gradient exhibits only little variation. During the I-phase, the outer E_r gradient steepens gradually and $E_{r,min}$ reaches values of approximately −15 kV/m. These $E_{r,min}$ values have been observed previously at the H-mode onset at AUG.[73,74] In the H-mode, $E_{r,min}$ values of −20 to −28 kV/m are reached, which are typical values for AUG H-modes.[61] At the same time as $E_{r,min}$ deepens, $E_{r,max}$ in the SOL increases slightly from L-mode to H-mode, where the radial positions of the two extremes are relatively constant.

B. Unfavorable drift configuration

Figure 5 shows a typical L-I-H transition in a LSN unfavorable drift configuration discharge (AUG #37298). This discharge is the equivalent to the previously presented favorable drift L-H transition discharge shown in Fig. 4. In #37298, the I-mode (red in Fig. 5) starts at around 2.68 s and is soon after followed by the H-mode (dark red) at around 2.77 s. At both confinement transitions (L-I and I-H) $P_{net} \approx 3$ MW, which is more than a factor of 2 higher than the corresponding P_{LH} in favorable drift configuration (see Fig. 3). Please note that P_{net} at the I-H transition often tends to be lower compared to P_{net} at the L-I transition, which was already reported in earlier I-mode studies at AUG.[69] This can be attributed to a lower Ohmic power in the I-mode, due to a higher plasma temperature, and to a stronger change of W_{MHD} at the L-I transition. Both terms contribute to P_{net} via Eq. (9).

In the following, we report on general features of the development of the edge profiles during the L-I-H transition, which have been observed to be the same regardless of the exact plasma configuration (LSN or USN unfavorable drift), the plasma density, and the type of applied heating power. As can be seen in Fig. 5(b), $T_{e,edge}$, $T_{i,edge}$, and W_{MHD} (cyan, orange, and green) start to increase at the L-I transition, whereas the plasma density (blue) stays rather constant and only starts to rise at the I-H transition. Correspondingly, $(\nabla_r p_i)/(en_i)$ steepens gradually from L- to I- to H-mode. Also E_r follows this trend, but in the L-mode (light red), discrepancies between $(\nabla_r p_i)/(en_i)$ and E_r are observed, as has been also found in the favorable drift configuration. The measurements show that the edge E_r profiles can be entirely positive in unfavorable drift L-modes, and, thus, $v_{E\times B}$ points then in the ion diamagnetic drift direction. This observation will be discussed in more detail in Sec. VI A. In the I-mode, $E_{r,min}$ deepens gradually and at values of approximately −15 kV/m the transition into the H-mode occurs, consistent with previous I-mode studies.[75] Interestingly, this $E_{r,min}$ value is about the same as $E_{r,min}$ values reached during the I-phase at the transition into the H-mode in favorable drift configuration plasmas.[4] However, this very similar $E_{r,min}$ value does not imply that the same outer E_r gradients are reached at the H-mode onset, since the E_r values in the SOL and their radial position can also be different. This is at least the case for the here presented discharge pair in favorable and unfavorable drift configuration (compare Figs. 4 and 5).

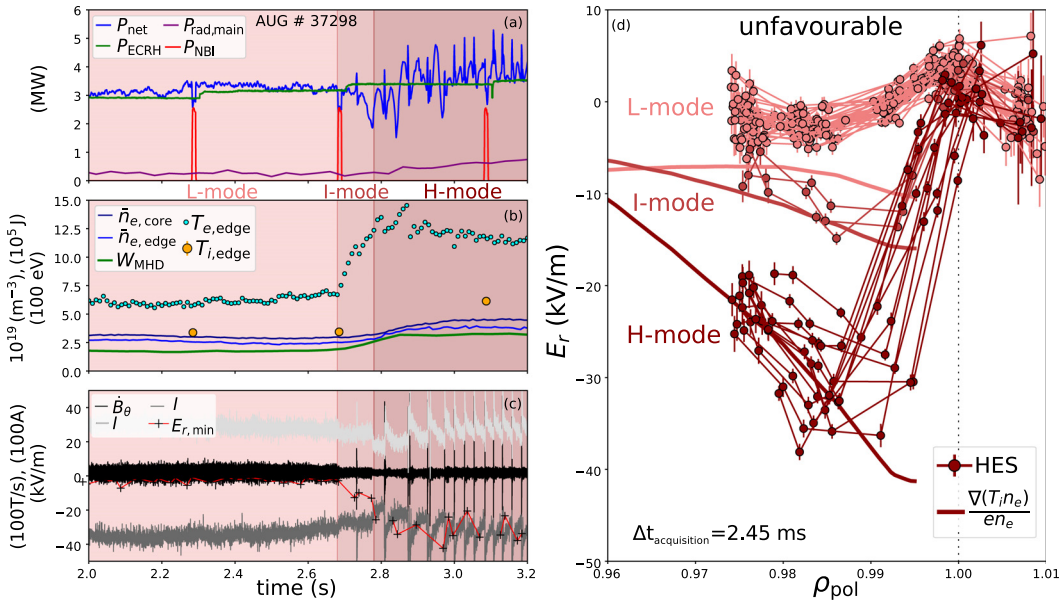

FIG. 5. Evolution of the L-I-H transition in the unfavorable drift configuration. Time traces of (a) NBI and ECRH power (red, green), net input power (blue), and main chamber radiation (purple) during an L-I-H transition. Corresponding evolution of (b) line-averaged electron density in the plasma core and edge (dark blue, blue), stored plasma energy (green), edge electron and ion temperature (cyan and orange) and (c) magnetic field fluctuations (black), inner and outer shunt current signals (silver and gray) and the minimum of the edge radial electric field (red). (d) Evolution of the outer E_r gradient and $(\nabla_r p_i)/(en_i)$ at the plasma edge during the L-I-H transition.

VI. COMPARISON OF L-MODES IN DIFFERENT DRIFT CONFIGURATIONS AT THE SAME HEATING POWER AND THE SAME PLASMA DENSITY

In order to understand the differences and similarities of edge kinetic and E_r profiles as well as the SOL conditions of L-mode plasmas in the two different drift configurations and to study their impact on the transition into an improved confinement regime, pairs of favorable/unfavorable L-modes with matched parameters, i.e., same heating power and same plasma density, are compared in this section. First we investigate LSN plasmas at low density and then USN plasmas at medium density. Based on the observed differences, conclusions are drawn on which mechanisms could be possible candidates to influence E_r in the L-mode.

A. Lower single-null and low density

In the two investigated L-mode phases, a gas puff rate $\Gamma_D \approx 0.7 \times 10^{21}$ el/s was used, which results in a plasma density of about 2.8×10^{19} m^{-3}. However, as can be seen in Fig. 6(b), the edge density is slightly lower in the unfavorable drift case (#37375, light red) compared to the favorable drift case (#36983, blue). Furthermore, in both L-mode phases, $P_{ECRH} = 600$ kW, which is for the favorable drift configuration directly before the L-H transition.

1. Edge kinetic and E_r profiles

Figure 6 shows the measured edge electron and ion kinetic profiles and the toroidal rotation and E_r profiles for the two L-mode phases. The edge T_e profiles are the same in favorable and unfavorable drift configurations, whereas n_e is slightly lower in the unfavorable drift configuration between $\rho_{pol} = 0.95$ and 0.98. The logarithmic edge density gradient, $1/L_{n_e} := -(\nabla_r n_e)/n_e$, is found to be the same within the measurement uncertainties in the confined plasma region. Also the T_i profiles agree within the measurement uncertainties, which leads to very similar $(\nabla_r p_i)/(en_i)$ profiles in favorable and unfavorable drift configuration [see Fig. 6(f)].

In both drift configurations, the edge T_i profiles are flatter than the edge T_e profiles, which is regularly observed. The ratio of $T_{i,sep}/T_{e,sep}$ is the same for either drift configuration and $T_{i,sep} \approx 100$ eV $= 1.3\, T_{e,sep}$ in both cases. According to Manz *et al.*,[15] a transition from ITG-dominated to Drift–Alfvén turbulence can take place if a sufficiently high $T_{i,sep}/T_{e,sep}$ or a rather low ∇T_i is reached at the separatrix, which then would lead to the existence of the I-mode. The observation here that $T_{i,sep}/T_{e,sep}$ and ∇T_i are very similar in both drift configurations, whereas the I-mode is absent in the favorable drift configuration, is in variance to the theory proposed by Manz *et al.*[15]

The impurity intrinsic toroidal rotation $v_{\phi,imp}$, which is the toroidal rotation without external torque input, is found to be almost the same and co-current in both drift configurations. This observation is in contrast to intrinsic edge rotation measurements in L-modes of favorable and unfavorable drift configurations in Alcator C-Mod,[1] which is observed to change with the drift configuration. A more detailed discussion on this can be found in Sec. VII C. Qualitative differences in the profiles shown in Fig. 6(e) might originate from the fact that the impurity rotation was measured on different impurities (B and N, respectively). Furthermore, although the external torque input by NBI is minimized by the short duration of the NBI blip, a small effect on v_ϕ cannot be excluded, even more since in the LSN favorable drift configuration, the NBI injection is co-current at AUG,

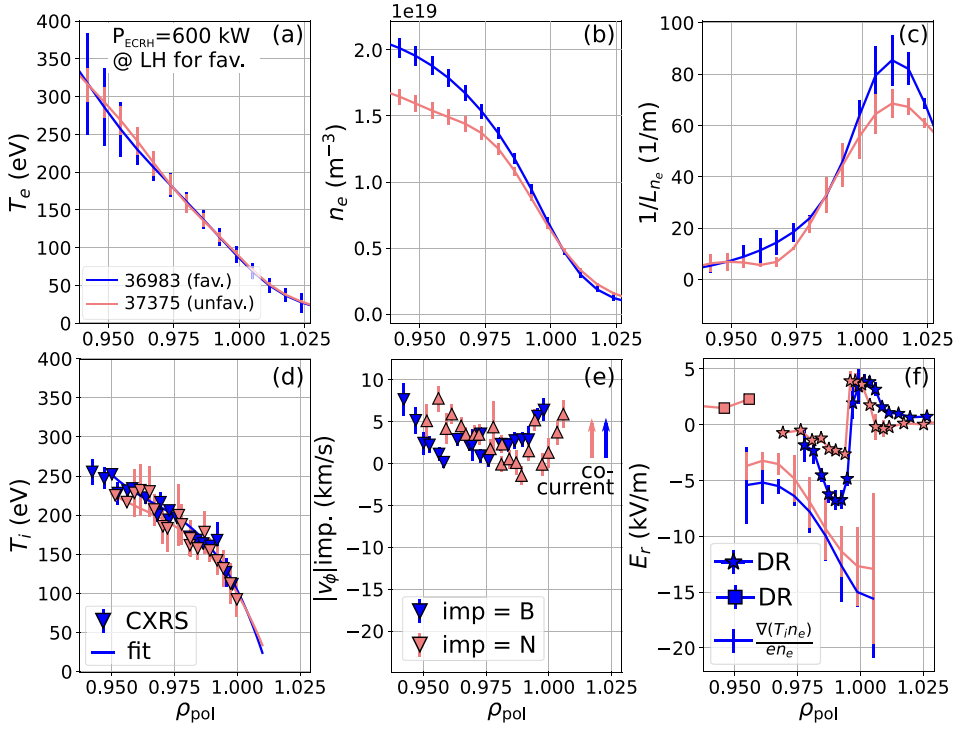

FIG. 6. Edge kinetic profiles of L-modes in favorable and unfavorable drift configuration at matched parameters. Radial profiles of measured (a) electron temperature T_e, (b) electron density n_e, (c) logarithmic electron density gradient $1/L_{n_e}$, (d) ion temperature T_i, (e) intrinsic toroidal rotation of impurities $v_{\phi,imp}$, and (f) radial electric field E_r as well as main ion pressure gradient $(\nabla_r p_i)/(en_i)$ (assuming $n_i = n_e$) for favorable (blue) and unfavorable (light red) drift configurations.

whereas it is countercurrent in the LSN unfavorable drift configuration (see Fig. 24).

The biggest difference between the two drift configurations is found in the measured edge E_r profiles. Although the slopes of the inner and outer E_r gradients can vary somewhat, e.g., due to heating method, a robust observation is that the E_r well in the confined region is shallower in unfavorable compared to favorable drift configuration. Thus, these new measurements confirm earlier studies at AUG and DIII-D[10,76] and recent results from the WEST tokamak.[12] As shown in Fig. 6(f), the $E_{r,\min}$ value for the unfavorable drift configuration case is less negative than the one in the favorable drift configuration, leading to a weaker inner E_r gradient in the unfavorable drift configuration. The $E_{r,\max}$ values are generally not very different between the two drift configurations; however, it is regularly observed that $E_{r,\max}$ is located just inside the separatrix for the unfavorable drift configuration, whereas it is located outside the separatrix for the favorable drift configuration. This causes that the outer E_r gradients are of similar strength between the two drift configurations.

2. Scrape-off layer profiles

Figures 7(a) and 7(b) show electron temperature and density profiles of the outer divertor target ($T_{e,\text{target}}$ and $n_{e,\text{target}}$) in favorable (blue) and unfavorable (light red) drift configurations. Also shown in the plots are $T_{e,\text{OMP}}$ and $n_{e,\text{OMP}}$, which were already presented in Fig. 6. The strong reduction of T_e along the field lines with a concomitant increase in n_e toward the divertor target ($p_{e,\text{OMP}} \approx 2p_{e,\text{target}}$ within the measurement uncertainties) indicates that the SOL plasma is in the conduction-limited regime. This, in turn, implies that the Spitzer–Härm power balance can be applied for the determination of the separatrix temperature at the OMP, as was done for all discharges in this work (see Sec. III).

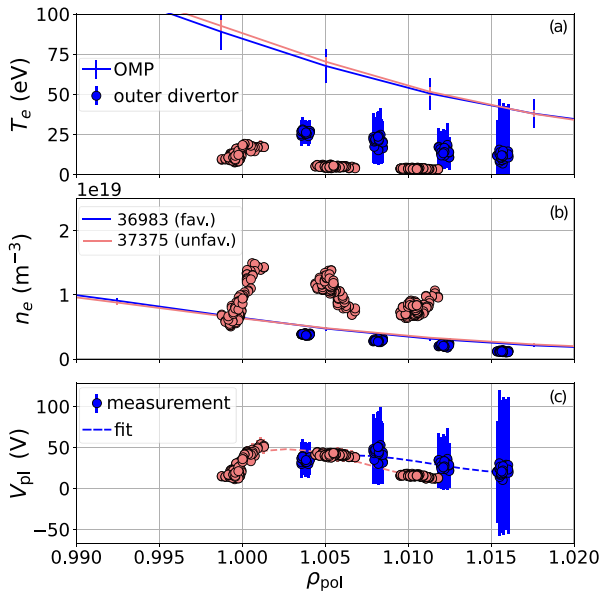

FIG. 7. SOL profiles in favorable and unfavorable drift configuration L-modes at matched parameters. Radial profiles of measured (a) electron temperature T_e, (b) electron density n_e at the outer target (circles) and at the outer midplane (OMP, lines) for favorable (blue) and unfavorable (light red) drift configurations. (c) Plasma potential V_{pl} at the OMP (circles), reconstructed from LP measurements at the outer target, and spline fit to the experimental data (dashed line).

As expected from a reversal of the drift directions in the SOL, the particle transport toward the outer divertor is increased in the unfavorable drift configuration compared to the favorable drift configuration, leading to a lower $T_{e,\text{target}}$ and a higher $n_{e,\text{target}}$ in unfavorable compared to the favorable drift configuration.[13,77–82] In the favorable drift configuration, $T_{e,\text{OMP}} \approx 3T_{e,\text{target}}$, whereas in the unfavorable drift configuration, $T_{e,\text{OMP}} > 3T_{e,\text{target}}$. In the unfavorable drift configuration, where the target profiles are fully resolved, $T_{e,\text{target}}$ peaks at the separatrix, while the maximum value of $n_{e,\text{target}}$ is reached a bit further outside in the SOL, at $\rho_{\text{pol}} \approx 1.001$. This is observed regularly and also theoretically predicted due to diffusive processes in the private flux region.[26,83]

The plasma potential at the OMP, reconstructed from the LP data at the outer divertor target, is shown in Fig. 7(c). The dashed lines are cubic spline fits to the experimental data. Although the absolute values are similar in both drift configurations, with V_{pl} between 0 and 60 eV, the profile shapes differ. In the unfavorable drift configuration, the peak of V_{pl} is narrow and occurs close to the separatrix, at around $\rho_{\text{pol}} = 1.002$, whereas in the favorable drift configuration, the peak is broader and exhibits its maximum at $\rho_{\text{pol}} \approx 1.007$. This qualitatively different behavior of V_{pl} for the different drift configurations has been observed also in other plasma discharges of similar plasma parameters, in which fully radially resolved target profiles were available also for the favorable drift configuration. The analysis of those data showed consistently that the maximum in $T_{e,\text{target}}$ does not exceed 30 eV and that the maximum value of V_{pl} is indeed reached at around $\rho_{\text{pol}} = 1.007$ in the favorable drift configuration.

The upstream E_r profiles reconstructed from the target profiles using Eq. (6) are depicted as dashed lines in Fig. 8 for the two drift configurations. For comparison, also the respective E_r measurements and $-\nabla_r T_{e,\text{OMP}}/e$ profiles [see Eq. (8)] are plotted. The measured SOL E_r profiles agree well with the $-\nabla_r T_{e,\text{OMP}}/e$ profiles around $E_{r,\max}$, but the decay of the measured E_r profiles in the SOL is faster than that of $-\nabla_r T_{e,\text{OMP}}/e$. The full reconstruction of E_r from $-\nabla_r V_{\text{pl}}$ agrees less with the experimental E_r profiles, in particular, for the unfavorable drift configuration. This discrepancy suggests that the simple SOL model lacks important effects, e.g., from cross field transport, in order to reproduce the upstream SOL E_r profile from the divertor profiles correctly. It could also be that the assumptions on the shape of p_e along the field lines have to be adapted or that $j_\parallel/\sigma_\parallel$ is in fact not negligible. This will be further investigated in the future. However, considering the large radial uncertainties around the separatrix, which are critical when aligning the target and upstream profiles for the SOL E_r reconstruction, the deduced E_r profiles from the target measurements are in reasonable qualitative and quantitative agreement with the measured E_r profiles at the OMP, at least in the favorable configuration. A more systematic experimental study at AUG in favorable drift configuration L-modes confirms this.[27]

Despite different outer divertor target profiles, the measured upstream SOL E_r profiles are very similar between the two drift configurations. This makes an explanation of the increased H-mode power threshold in the unfavorable drift configuration due to a weaker SOL E_r hill and, thus, due to a significantly weaker outer E_r gradient implausible, as it was suggested previously based on SOL modeling results.[13,14]

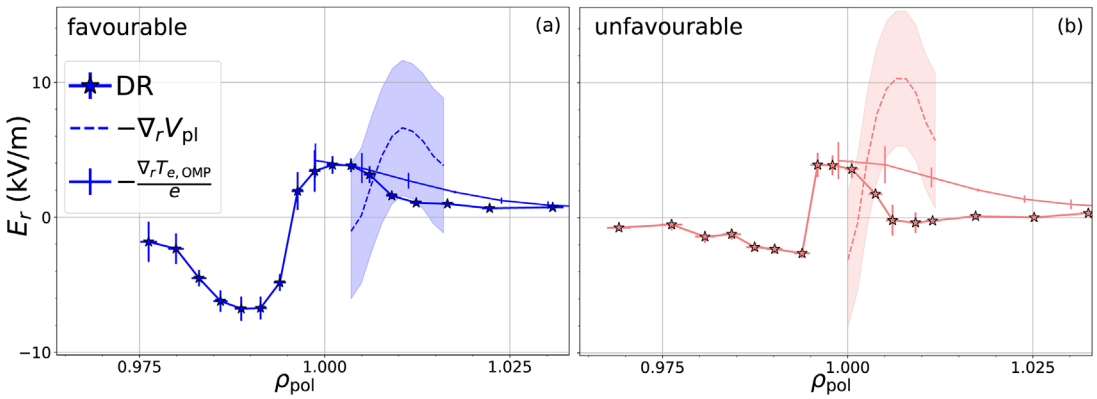

FIG. 8. SOL E_r profiles in favorable and unfavorable drift configuration L-modes at matched parameters. Measured E_r profiles at the OMP (stars) in comparison with the reconstructions of E_r from target profiles, using $E_r = -\nabla_r V_{pl}$ (dashed line), and the approximation for the conduction-limited regime $E_r \approx -\nabla_r T_{e,OMP}$ (solid line) for favorable (a) and unfavorable (b) drift configurations.

3. Neoclassical calculations

In this section, the experimental E_r profiles shown in Fig. 6(f) are compared to NEOART calculations (see Sec. III F). This comparison helps to clarify whether the observed differences in E_r between the two drift configurations are due to NC effects. As input for the NC predictions of $v_{\theta,i}$, $v_{\theta,\mathrm{imp}}$, and $v_{\phi,i}$, the experimental n_e, T_e, T_i, and $v_{\phi,\mathrm{imp}}$ profiles presented in Figs. 6(a)–6(e) were used. The resulting velocity profiles are shown in Fig. 9. For completeness, also the measured $v_{\theta,\mathrm{imp}}$ and $v_{\phi,\mathrm{imp}}$ data from CXRS as well as the fits to the $v_{\phi,\mathrm{imp}}$ profiles are shown.

In both drift configurations, the measured intrinsic $v_{\phi,\mathrm{imp}}$ and the predicted $v_{\phi,i}$ are co-current and the predicted NC poloidal impurity and main ion velocities are in the electron diamagnetic drift direction close to the separatrix. The experimental data of $v_{\theta,\mathrm{imp}}$ and the NC predictions are in reasonable agreement, which indicates that also the main ion predictions are reliable.

Inserting the toroidal and poloidal main ion velocity and the $(\nabla_r p_i)/(en_i)$ profiles from NEOART into the radial force balance equation [Eq. (3)] gives an estimate for the size and shape of the edge E_r based on local NC theory. Since it was found that the resulting predicted E_r profiles depend sensitively on the input T_i data, a discussion on this dependence can be found in Appendix B. The conclusions from this sensitivity study is that the shape of the predicted E_r profile depends strongly on the input T_i profile; however, the differences found in E_r between favorable and unfavorable drift configurations are independent of the choice of the T_i profile fit. Therefore, in Fig. 10, a comparison of the predicted E_r profile (solid line), $(\nabla_r p_i)/(en_i)$ only (dashed line), and the experimental E_r profile (stars) for favorable (blue) and unfavorable (light red) drift configurations is shown for the "flat T_i fit" (see also Appendix B).

In both drift configurations, the experimental E_r profiles agree better with the predicted E_r profiles including the main ion velocities, than with solely the $(\nabla_r p_i)/(en_i)$ profile. This gives evidence that the $v_i \times B$ contribution to E_r is not negligible in the L-mode, as has already been shown at DIII-D.[24,84,85] At AUG in the here investigated L-modes, it is actually found that the contributions of $(\nabla_r p_i)/(en_i)$, $v_{\phi,i}B_\theta$ and $v_{\theta,i}B_\phi$ are of comparable size, but they can have different signs and, therefore, they can cancel each other out and counteract each other.

As can be seen in Fig. 10, for the favorable drift configuration, the predicted E_r profile agrees with the experimental data quantitatively in the region around $E_{r,\mathrm{min}}$, whereas for the unfavorable drift configuration, larger differences between the predicted E_r profiles and the experimental profiles are found. Qualitative agreement of the profile shape between predicted and experimental E_r is only found for the favorable drift configuration using the "steep T_i fit" (see Appendix B), for which

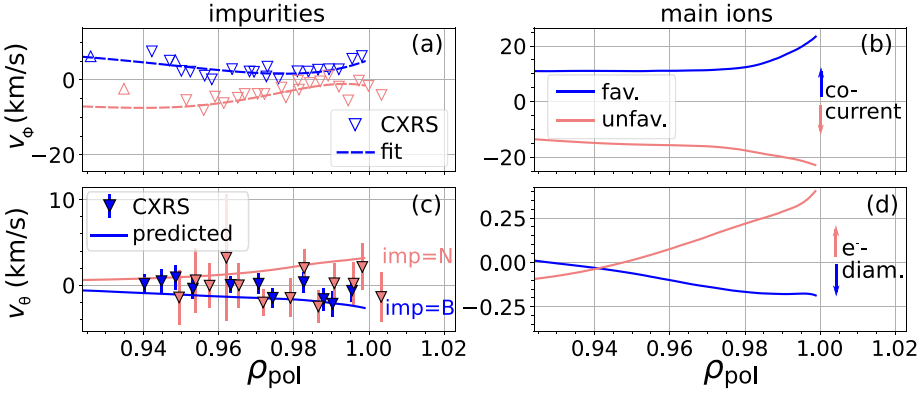

FIG. 9. Neoclassical and experimental edge velocities in L-mode plasmas of matched parameters in favorable and unfavorable drift configurations. (a) Measured intrinsic toroidal impurity rotation (triangles) and fit to the experimental data (dashed line), (b) predicted intrinsic toroidal main ion rotation, (c) measured (triangles) and predicted (solid line) poloidal impurity velocity, and (d) poloidal main ion velocity profiles of favorable (blue) and unfavorable (light red) drift configurations.

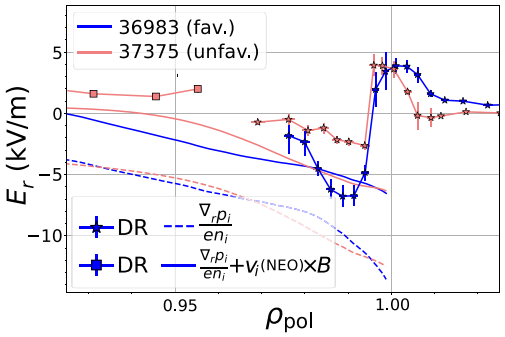

FIG. 10. Comparison of exp. E_r profiles with neoclassical predictions in favorable and unfavorable drift configuration L-modes of matched parameters. Predicted E_r profiles from NEOART including main ion velocities (solid lines) and main ion pressure gradient profiles only (dashed lines) and experimental edge E_r profiles (stars, squares) for favorable (blue) and unfavorable (light red) drift configurations. Figure adapted from Plank *et al.*, Plasma Phys. Controlled Fusion **65**, 014001 (2023). Copyright 2023 Author(s), licensed under a Creative Commons Attribution (CC BY) license.

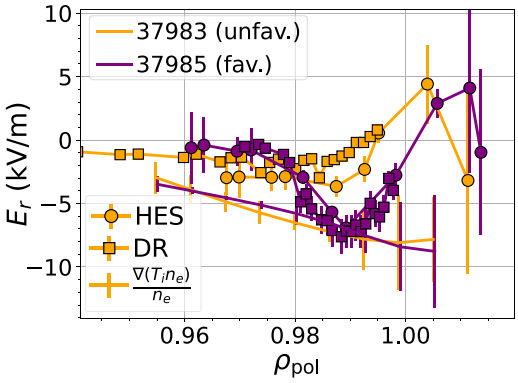

FIG. 11. Comparison of L-modes in favorable and unfavorable drift configurations at matched parameters. Edge radial electric field profiles from DR (squares) and HES (circles) and main ion pressure gradient profile (solid lines) for USN favorable (purple) and unfavorable (orange) drift configurations.

a minimum in the predicted E_r profile can be produced. However, it is not a general result that NC predictions of E_r agree better with experimental data in favorable compared to the unfavorable drift configuration. As shown in Sec. VI B, counter examples exist.

B. Upper single-null and medium density

Several pairs of L-H (L-I-H) transition discharges with identical ECRH power ramps and a plasma density of $\bar{n}_e = 4.5 \times 10^{19}\mathrm{m}^{-3}$ were performed also in USN favorable and unfavorable drift configurations. These discharges were density feedback-controlled and operated with $|B_\phi| = 2.5\,\mathrm{T}$ at the geometric axis, $I_\mathrm{p} = 1.0\,\mathrm{MA}$ and $|q_{95}| = 3.8$. Two example L-mode phases are presented in the following, which were both heated with $P_{\mathrm{ECRH}} = 200\,\mathrm{kW}$. This phase is, for the favorable drift configuration discharge #37985, right before the L-H transition, but still long before the L-I transition for the unfavorable drift configuration discharge #37983 ($P_{\mathrm{ECRH}} \approx 1.4\,\mathrm{MW}$ at L-I). Due to the lower coverage of the upper divertor with LP measurements at AUG, no divertor target profiles are available for these discharges.

1. Edge E_r profiles

In Fig. 11, the measured L-mode E_r profiles for favorable (purple) and unfavorable (orange) drift configuration are plotted together with the experimental $(\nabla_r p_i)/(en_i)$ profiles, assuming $n_i = n_e$ for the latter. Due to the higher density of these discharges, the E_r measurements by DR are restricted to the confined region. Therefore, HES measurements of the outer E_r gradient are also shown in the figure. As can be seen, the E_r profiles from both diagnostics are in good agreement, although for the unfavorable drift configuration deviations of up to 2 kV/m are observed between the two diagnostics.

The edge electron and ion kinetic profiles are very similar in both drift configurations, leading to almost identical $(\nabla_r p_i)/(en_i)$ profiles. In contrast to $(\nabla_r p_i)/(en_i)$, the E_r profiles are different between the two drift configurations, where the E_r well in the confined region is again shallower in the unfavorable drift configuration, which also causes the inner E_r gradient to be significantly weaker in unfavorable compared to the favorable drift configuration, whereas the outer one is of comparable strength.

In summary, these observations are the same as for the pair of low density L-modes in LSN favorable and unfavorable drift configurations described in Sec. VI A. A difference to the LSN L-modes at low density is that in the L-modes presented here, the intrinsic $v_{\phi,\mathrm{imp}}$ (measured on B) is slightly higher in favorable compared to the unfavorable drift configuration [see Fig. 12(a)], but it is again co-current for both drift configurations.

2. Neoclassical calculations

In Fig. 12, the impurity and main ion velocities are shown for the two drift configurations as predicted by NEOART. The intrinsic toroidal main ion rotation (b) is co-current for both drift configurations, but, as the measured $v_{\phi,\mathrm{imp}}$ (a), $v_{\phi,i}$ is larger in the favorable drift configuration. The predicted NC impurity (c) and main ion (d) poloidal velocities are of comparable size between the two drift configurations, and point for either configuration into the electron diamagnetic drift direction. The experimental $v_{\theta,\mathrm{imp}}$ data exhibit a large scatter, but they rather agree with the NC predictions for the unfavorable drift configuration. In the favorable drift configuration, the experimental $v_{\theta,\mathrm{imp}}$ data point into the ion diamagnetic drift direction. Accordingly, see Fig. 13, the predicted E_r profile employing NC main ion velocities (solid line) agrees better with the experimental E_r profile for the unfavorable (orange) than for the favorable drift configuration (purple). For the latter, the predicted E_r profile is much less negative than the experimental data and also the steep inner E_r gradient cannot be resolved. A comparable flat inner E_r gradient, as the predicted E_r profiles exhibit, is only found for the experimental E_r profile in the unfavorable drift configuration.

The main reason for the less negative E_r profile prediction by NC theory in favorable compared to the unfavorable drift configuration, which is opposite to the experimental observation, is mainly due to the differences in the measured $v_{\phi,\mathrm{imp}}$. The latter has consistently been found to be larger in favorable than in unfavorable drift configuration in several USN discharges. As stated before, this difference in the E_r

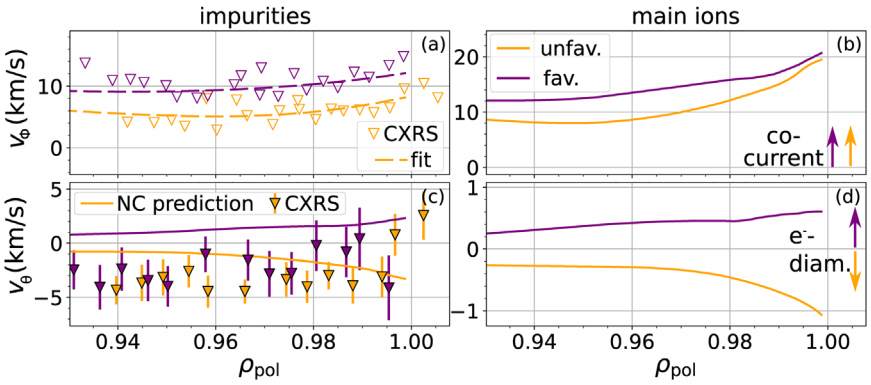

FIG. 12. Neoclassical velocity profiles in favorable and unfavorable drift configuration L-modes of matched parameters. (a) Toroidal intrinsic impurity rotation profile (triangles) and fit of the data (dashed lines), (b) predicted toroidal intrinsic main ion rotation, (c) predicted neoclassical poloidal impurity velocity (solid lines), and experimental data (triangles) and (d) predicted neoclassical poloidal main ion velocity for favorable (purple) and unfavorable (orange) drift configurations.

predictions can also not be resolved by steeper T_i gradient fits to the experimental data (see also Appendix B).

Please note, the strong deviations between the predicted and the experimental E_r profiles, which are present in the region of the outer E_r gradient between $\rho_{pol} \approx 0.98$ and 1.0, are likely due to other contributions to E_r, which have been assumed to be negligible, or they are not captured by local NC theory. These can be friction forces or non-isotropic pressure contributions [see Eqs. (1) and (2)] as well as ion orbit losses and global NC effects, which are not captured by NEOART. As shown in Sec. VII, in the region around the separatrix, also a strong interaction between confined plasma and SOL seems to be present.

C. Discussion of possible mechanisms influencing E_r

Comparison of L-mode phases with same heating power and same plasma density, but different drift configuration has shown that, although $(\nabla_r p_i)/(en_i)$ is very similar between the two drift configurations, the E_r well in the confined region is shallower in unfavorable compared to the favorable drift configuration. This leads to less steep E_r gradients in the unfavorable drift configuration, as has been observed previously.[10–12] This is found consistently regardless whether pairs of LSN or USN discharges are investigated, which implies that this effect is independent of the exact divertor geometry (closed or open divertor). In both drift configurations, it is found that E_r in the L-mode deviates from $(\nabla_r p_i)/(en_i)$, showing that $v_i \times B$ is a non-negligible contribution to E_r, as also observed previously at DIII-D.[24,84,85] Comparisons with local NC theory give better agreement in magnetic configurations in which B_ϕ is negative, i.e., clockwise seen from above (standard B_ϕ direction at AUG). This agreement is, in the discharges presented here, connected to favorable drift configuration in LSN and to unfavorable drift configuration in USN plasmas (see also Appendix A). However, in detail deviations of the measured E_r profiles from NC theory are found in either drift configuration, which is consistent with results from DIII-D in favorable drift configuration plasmas.[24] In particular, the NC predictions cannot reproduce the differences observed in E_r between the two drift configurations.

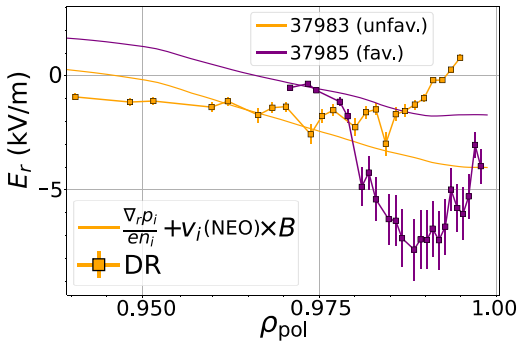

FIG. 13. Comparison of E_r profiles with neoclassical predictions in favorable and unfavorable drift configuration L-modes of matched parameters. Measured E_r profiles (squares) and NC predictions (solid lines) in favorable (purple) and unfavorable (orange) drift configurations.

Various mechanisms are discussed in the community that can lead to differences in the edge E_r, depending on the magnetic configuration. Possible candidates, which would be consistent with the experimental data, are a contribution of the magnetic-shear-induced Reynolds stress on the parallel momentum and, thus, E_r (Refs. 16, 86, and 87) or other turbulent stresses which modify the mean-field parallel and toroidal momentum transport.[17,88] In either cases, the observed differences in E_r would originate from differences in the momentum stresses due to the up-down asymmetry and/or the different helicity of the magnetic flux surfaces. Further possible effects on the intrinsic edge rotation and E_r in the confined plasma edge could originate from ion orbit losses or from interactions with neutrals.[89–91] Their impacts on the intrinsic edge v_ϕ and on the edge E_r also depend on the exact magnetic configuration.[19,20,90] First comparisons show that such effects are at least in qualitative agreement with experimental observations from AUG,[92,93] but further analysis and detailed comparisons are required to draw definitive conclusions. Moreover, it should be noted that the NC calculations in this work were purely local. However, close to the separatrix, in the region where the kinetic profile gradients are steep, also global effects, which are not treated in local calculations, could play an important role, as could be the case for some of the plasmas presented in this study. From theory, mainly a change of the poloidal main ion velocity at the plasma edge is expected, which is confirmed by comparisons of global to local NC simulations.[94] Such effects can as well influence the E_r predictions from NC theory. Comparisons of these different effects to the experimental data are currently undertaken or foreseen in the near future and are not object of this present work. It is important to note that for either of these effects, it has to be investigated carefully on how it

impacts the edge velocities and edge E_r profiles and whether it changes with the magnetic configuration, i.e., with the B-field direction and/or its helicity.

In conclusion, it can be stated that if the paradigm of the suppression of edge turbulence by a large enough $v_{E\times B}$ shear holds (see Sec. II), the observed differences in the E_r profiles in the confined plasma between the two drift configurations could explain the different H-mode power thresholds for the two drift configurations. In this framework, more heating power would be needed in the unfavorable drift configuration in order to reach a steep enough E_r gradient, via $\nabla_r T_i$, to suppress the edge turbulence, assuming that the latter is unchanged. However, as shown in the following, in the unfavorable drift configuration, it is not always found that the edge E_r gradients steepen as soon as the input power is increased, e.g., for low-density ECRH L-modes (see Sec. VII A). Furthermore, it is also not observed that similarly steep edge E_r gradients (neither the inner nor the outer E_r gradient) are reached at the respective H-mode transition for plasma pairs in favorable and unfavorable drift configurations. This is discussed in more detail in Sec. VIII.

VII. HEATING POWER AND PLASMA DENSITY SCANS IN UNFAVORABLE DRIFT CONFIGURATION L-MODES

In this section, constant phases of L-modes in LSN unfavorable drift configuration are compared, to study the evolution of the target profiles, the edge intrinsic toroidal rotation and E_r profiles in the L-mode, up to the confinement transition. The unfavorable drift configuration was chosen since, due to the larger L-mode window, also larger variations in heating power and plasma density can be investigated. The dependencies of E_r on plasma density and heating power described in the following are, however, also found in favorable drift configuration L-modes. The investigated L-mode phases of the AUG discharges #37375, 37298, 35753, and 35758 had either the same plasma density of $\bar{n}_e \approx 2.7 \times 10^{19}\mathrm{m}^{-3}$ and were heated with $P_{\mathrm{ECRH}} = 0.60$, 2.9, and 4.0 MW (see Sec. VII A) or constant ECRH power was applied ($P_{\mathrm{ECRH}} = 2.9$ MW), but the density was increased from $\bar{n}_e = 2.5$ to 4.0 and $6.0 \times 10^{19}\mathrm{m}^{-3}$ (see Sec. VII B).

A. Different heating power at constant plasma density

1. Edge profiles

Figure 14 shows the edge electron and ion kinetic profiles for the L-modes phases heated with different amounts of ECRH power. As expected, T_e increases with increasing P_{ECRH} and for the highest heating power of 4.0 MW $T_{e,\mathrm{sep}} \approx 130$ eV, according to Spitzer–Härm power balancing (see Sec. III D). Such a high $T_{e,\mathrm{sep}}$ is, in favorable drift configuration plasmas, observed in H-modes only. Also T_i increases with increasing ECRH power, whereas n_e and $1/L_{n_e}$ vary only slightly. The edge $(\nabla_r p_i)/(en_i)$ profiles, shown in Fig. 15(b), are the same, within the uncertainties, for all three different L-mode phases. Power balance calculations for these L-modes have shown that $Q_{i,\mathrm{edge}}$ saturates at a value of about 0.6 MW and does not increase further with increasing P_{ECRH}. The reason for this saturation is that in pure electron heated plasmas energy to the ions is only transferred via equipartition. However, the equipartition power density $p_{ei} \propto n_e^2 \frac{T_e - T_i}{T_e^{3/2}}$ is low in these L-modes due to the low plasma density and, for high enough T_e, p_{ei} decreases with increasing T_e. Thus, the critical $Q_{i,\mathrm{edge}}$ needed to enter I-mode in these plasma conditions at AUG is, according to Ryter *et al.*,[69] not reached.

The measured impurity's intrinsic toroidal edge rotation (here N) is shown in Fig. 15(a). For all three L-mode phases, it is co-current and it increases in size with increasing P_{ECRH}. Accordingly the edge E_r becomes less negative (even becomes positive) with increasing P_{ECRH} [see Fig. 15(b)] in the confined plasma but also shifts upwards by

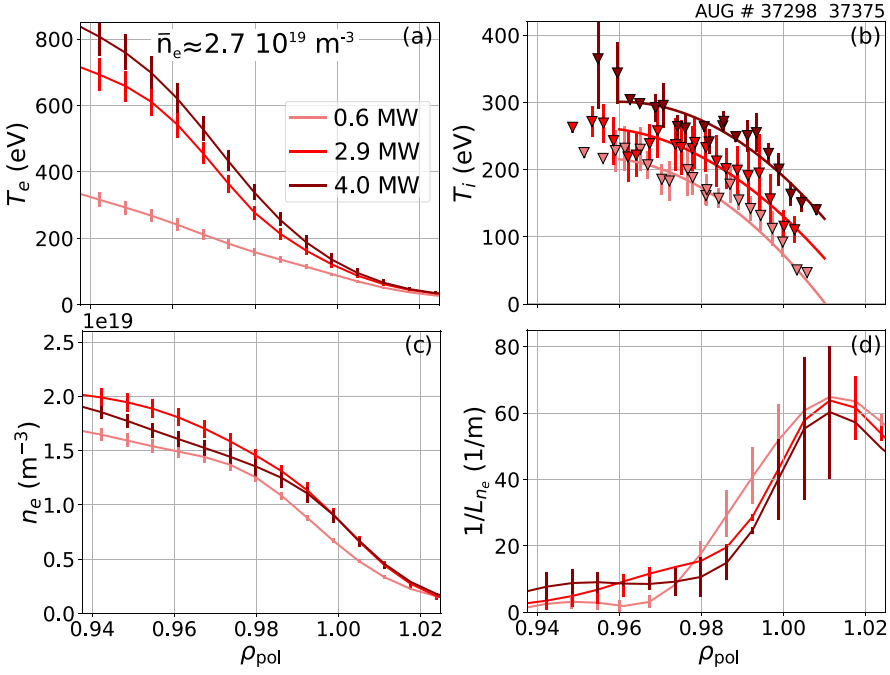

FIG. 14. Edge kinetic profiles of L-modes with same plasma density and different ECRH power in the unfavorable drift configuration. Experimental radial profiles of the edge (a) electron temperature, (b) ion temperature, (c) electron density, and (d) logarithmic electron density gradient.

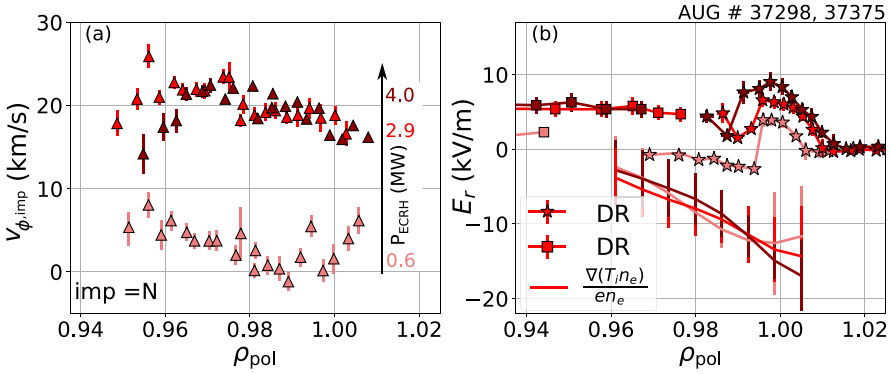

FIG. 15. Edge rotation and E_r profiles of L-modes with same plasma density and different heating power in the unfavorable drift configuration. Profiles of the measured (a) intrinsic impurity edge rotation and (b) edge radial electric field (stars and squares), together with the approximation ($n_i = n_e$) of the main ion pressure gradient (solid lines).

about the same amount in the SOL, leaving the outer E_r gradient almost unchanged. For the two higher heating power phases, $v_{E\times B}$ points into the ion diamagnetic drift direction, since $E_r > 0$. Again, the experimental E_r profiles deviate strongly from $(\nabla_r p_i)/(en_i)$ in the confined plasma, which exhibits a minimum value of about −15 kV/m. This indicates that the flow velocity terms are significant and responsible for the shift to positive E_r as shown in Sec. VII A 2.

2. Neoclassical calculations

A comparison of the experimental E_r profiles with the NEOART predictions is shown in Fig. 16. The predicted E_r profiles are more negative than the measured ones, particularly for the lowest heating case (light red), but the relative changes of E_r with increasing heating power are reproduced. They also show that the edge E_r profile becomes positive with higher P_{ECRH}. In conclusion, the comparison between experiment and NC predictions confirms that the NC contribution of $v_i \times B$ to E_r is not negligible and $(\nabla_r p_i)/(en_i)$ cannot be used as a proxy for E_r in the L-mode. The E_r measurements also reveal that the E_r gradients do not steepen with increasing heating power in these plasma conditions, which could explain the high P_{LH} in such types of plasmas (low density plasmas heated with ECRH)[48,73] and the observation that the here presented discharges did not enter an improved confinement regime. As stated before, the deviations between the predictions of local NC theory and experimental data, which is an approximately constant offset of 2–4 kV/m in the ion diamagnetic drift direction, indicate that other effects also contribute to E_r, which are not included in the NEOART calculations. However, it is not clear as of yet which are the (additional) mechanisms influencing the poloidal and/or toroidal velocity and, thus, E_r. This will be addressed in future work. Several candidates can be considered, which were already presented in Sec. VI C.

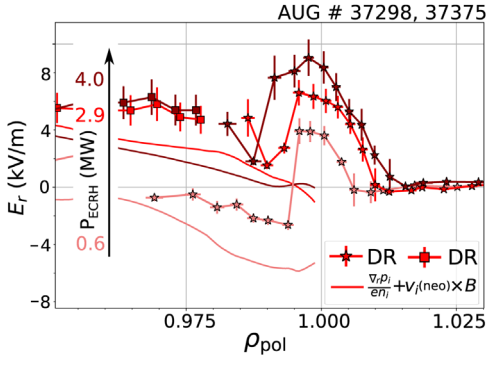

FIG. 16. Comparison of E_r profiles with neoclassical predictions in unfavorable drift configuration L-modes of same plasma density at different ECRH powers. Measured E_r profiles (squares and stars) and NC predictions (solid lines).

3. SOL E_r profiles

Figure 17 shows again the measured upstream E_r profiles, now in comparison with the two different SOL models. As stated before, $E_{r,\max}$ increases with increasing ECRH power and the same trend is found for the two estimates of the upstream E_r, $-\nabla_r T_{e,\mathrm{OMP}}/e$ and $-\nabla_r V_{\mathrm{pl}}$ [see Eqs. (8) and (7)]. As has been mentioned before (see Sec. VI A 2), the experimental data agree quantitatively better with $-\nabla_r T_{e,\mathrm{OMP}}/e$, whereas $-\nabla_r V_{\mathrm{pl}}$ overestimates E_r in the SOL.

B. Same heating power and different plasma density

1. Edge profiles

Figure 18 shows the edge electron and ion kinetic profiles of the L-mode density scan at constant ECRH power. According to Spitzer–Härm power balancing, $T_{e,\mathrm{sep}}$ is constant, independent of the edge density, which is consistent with a conduction-limited SOL.[26,56] Also T_i stays rather constant and shows only a very weak decrease with increasing n_e, as well as $1/L_{n_e}$, which does not change with increasing n_e. Bigger changes with varying L-mode density are found for the experimental intrinsic toroidal edge rotation profiles of nitrogen [see Fig. 19(a)]. With increasing plasma density $v_{\phi,\mathrm{imp}}$ decreases and even becomes countercurrent. This behavior is also consistently reflected in the edge E_r profiles [Fig. 19(b)]. $E_{r,\min}$ decreases with increasing n_e and $v_{E\times B}$ changes from the ion into the electron diamagnetic drift direction, in accordance with observations at DIII-D investigating the impact of edge rotation on the edge E_r and P_{LH} in the L-mode.[71,85]

It is interesting to observe that the radial electric field decreases both in the confined region and in the SOL, keeping the outer E_r gradient nearly constant. Also the inner E_r gradient does not steepen coherently with decreasing $E_{r,\min}$. This observation implies that $E_{r,\min}$ is not always a good proxy for its edge gradients in L-mode conditions, as

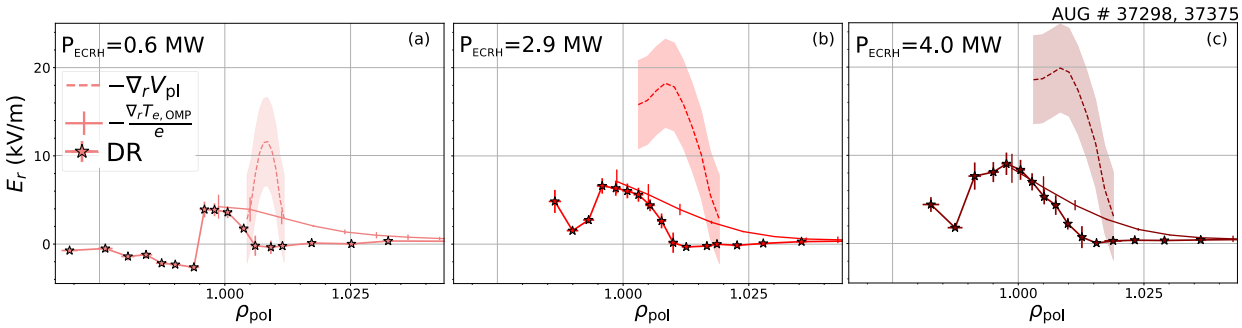

FIG. 17. SOL E_r profiles in unfavorable drift configuration L-modes of same plasma density at different ECRH powers. (a)–(c) Measured E_r profiles in the SOL (DR, stars) and different estimates of the upstream E_r in the SOL deduced from target profiles ($-\nabla_r V_{pl}$, dashed lines) and from the outer midplane profiles ($-\nabla_r T_{e,OMP}/e$, solid lines).

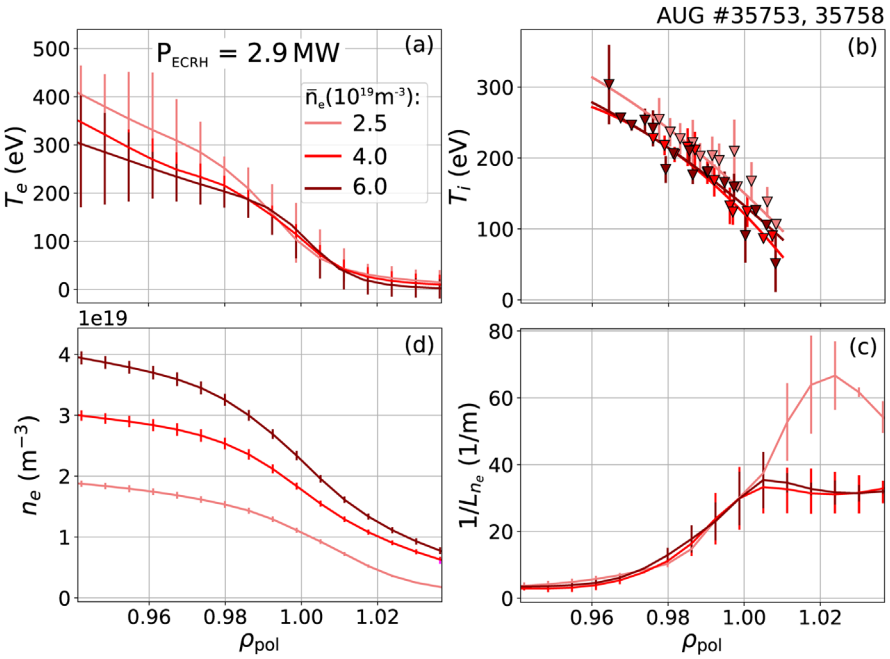

FIG. 18. Edge kinetic profiles in unfavorable drift configuration L-modes of different plasma densities at the same heating power. Experimental radial profiles of the edge (a) electron temperature, (b) ion temperature, (c) electron density, and (d) logarithmic electron density gradient.

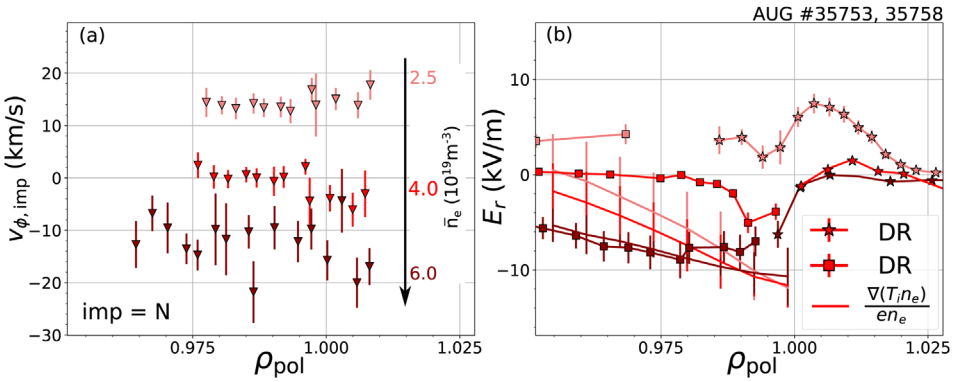

FIG. 19. Edge rotation and radial electric field profiles in unfavorable drift configuration L-modes of different plasma densities at the same heating power. Profiles of the measured (a) intrinsic impurity edge rotation and (b) edge radial electric field (stars and squares), together with the approximation ($n_i = n_e$) of the main ion pressure gradient (solid lines).

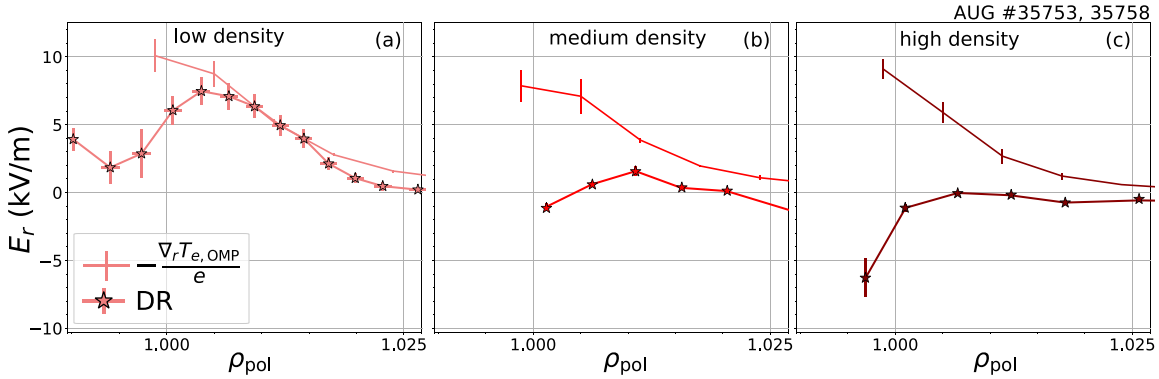

FIG. 20. SOL E_r profiles in unfavorable drift configuration L-modes of different plasma densities at the same heating power. (a)–(c) Measured E_r profiles in the SOL (DR, stars) and an estimate of the upstream E_r in the SOL based on electron temperature profiles at the outer midplane ($-\nabla_r T_{e,OMP}/e$, solid lines).

often assumed. $(\nabla_r p_i)/(en_i)$, which is always negative, is the same for all three different L-mode phases, and its minimum is about −12 kV/m. For the highest density L-mode, a quantitative agreement between E_r and $(\nabla_r p_i)/(en_i)$ is found, indicating that for this case, $v_i \times B \approx 0$, which is confirmed by NC calculations (see Sec. VII B 3). Furthermore, for this case, the E_r hill in the SOL disappears and E_r remains negative or close to 0 in the SOL. As can be seen in Fig. 20, in such conditions, the SOL E_r cannot be approximated by $-\nabla_r T_{e,OMP}/e$, since the latter is always positive (see Sec. VII B 2).

2. SOL E_r profiles

LP measurements at the outer divertor indicate that the target T_e decreases, whereas the target n_e increases with increasing plasma density. This trend is in line with the observation that the SOL E_r decreases at the OMP; however, the divertor measurements are not good enough in order to quantitatively reconstruct E_r in these three L-mode phases from target profiles. Recent studies at AUG in favorable drift configuration L-modes show that a reconstruction of $E_r = -\nabla_r V_{pl}$ from outer target measurements can reproduce the negative upstream E_r profiles, as they are observed for the highest density L-mode here.[27] In Fig. 20, a comparison of the measured upstream SOL E_r profiles with $-\nabla_r T_{e,OMP}/e$ is shown. While for the lowest density, the two profiles are in good agreement, $-\nabla_r T_{e,OMP}/e$ fails to reproduce the decrease in the SOL hill with increasing plasmas density. These deviations suggest that in unfavorable drift configuration plasmas, the simple SOL model introduced in Sec. II to deduce the upstream E_r in the SOL from outer midplane measurements is not sufficient and it neglects important mechanisms, which could lead to a qualitative and quantitative agreement. Possible modifications could come from parallel currents in the SOL, which are assumed to be small in our analytical model, but could become more important at higher densities.[26] Also, cross field transport is not included in the simple SOL model. To capture these effects correctly, more sophisticated SOL modeling would be required as it is included in the SOLPS code package.[95]

3. Neoclassical calculations

Figure 21 shows the E_r profiles, which were calculated with the main ion velocities as predicted by NEOART (solid lines) and the experimental E_r profiles (squares and stars) for the three different phases. The predicted E_r profiles reproduce qualitatively the changes in the experimental data with increasing plasma density, but a decent quantitative agreement between the experimental and the predicted E_r profile is only found for the L-mode phase with highest density, for which $v_{i,NEO} \times B \approx 0$.

C. Collisionality-dependence of intrinsic toroidal edge rotation and E_r and connection to SOL flows

Taking together the results from Secs. VII A and VII B, the intrinsic toroidal edge rotation and E_r increase with increasing P_{ECRH} and decrease with increasing n_e in AUG L-modes. This suggests a correlation between the intrinsic edge v_ϕ and the edge E_r with the electron or ion edge collisionality, ν_e^* or ν_i^*, since the latter two quantities are proportional to n_e/T_e^2 and n_i/T_i^2, respectively. Indeed, it has been already found at Tokamak à Configuration Variable (TCV) that the intrinsic toroidal edge rotation changes with density and temperature in L-modes, particularly in the unfavorable drift configuration.[96] The correlations between ion collisionality, the intrinsic toroidal edge rotation (multiplied by the local poloidal magnetic field, which is constant at $|B_\theta| \approx 0.33$ T for this data set), and the E_r profile across the separatrix

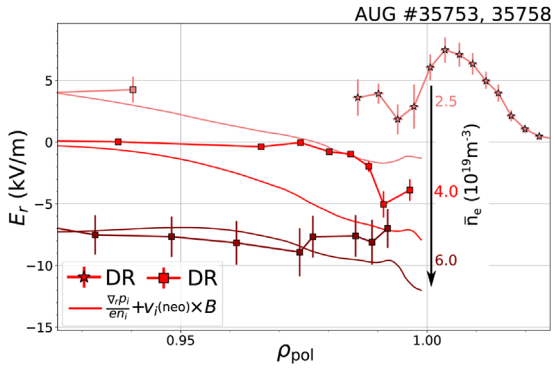

FIG. 21. Comparison of E_r profiles with neoclassical predictions in unfavorable drift configuration L-modes of different plasma densities at the same heating power. Measured E_r profiles (squares and stars) and NC predictions (solid lines).

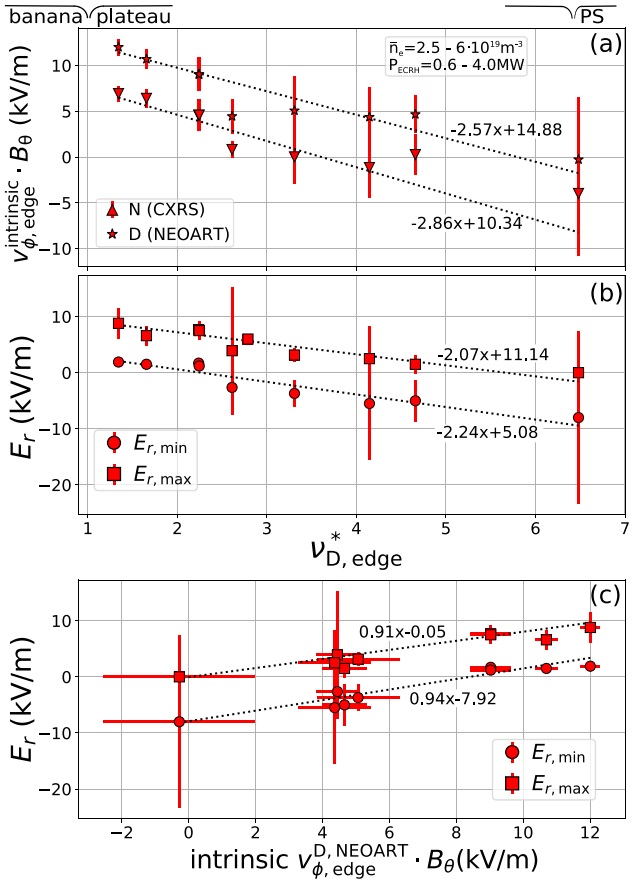

FIG. 22. (a) Measured intrinsic toroidal edge rotation of impurities (triangles) and predicted values for the main ions (stars) multiplied with the local poloidal magnetic field strength and plotted against the main ion collisionality. (b) $E_{r,\max}$ (squares) and $E_{r,\min}$ (circles), determined by DR and HES plotted against the main ion collisionality. The different collisionality regimes are indicated in the data (banana, plateau, Pfirsch–Schlüter). (c) $E_{r,\max}$ (squares) and $E_{r,\min}$ (circles) plotted against the toroidal main ion rotation, which was predicted using NEOART. The dotted lines are linear fits to the experimental data; their respective slopes and offsets are written in the plots.

are summarized in Fig. 22. Please note that these data originate from LSN unfavorable drift configuration plasmas only, but the same trends have been found in the other magnetic configurations as well.

For this figure, the collisionality of deuterium (main ion species) was calculated at $\rho_{\mathrm{pol}} = 0.98$. The different collisional regimes [banana, plateau, Pfirsch–Schlüter (PS)] are indicated at the top of the figure. The impurity intrinsic toroidal edge rotation $v_{\phi,\mathrm{imp}}$, evaluated at $\rho_{\mathrm{pol}} = 0.98$, was experimentally determined via CXRS, and the main ion rotation was inferred with NEOART. The minimum value of E_r in the confined plasma region ($E_{r,\min}$) and the maximum value of E_r in the SOL ($E_{r,\max}$) were taken from measurements (HES and DR).

As can be seen in Fig. 22(a), the intrinsic edge v_ϕ decreases linearly with increasing ν_i^*, where it is co-current in the banana-plateau regime, but starts to become countercurrent in the PS-regime. This dependency of the intrinsic edge v_ϕ on n_e and T_e (T_i) is also found in favorable drift configuration L-modes, although, due to the smaller L-mode window, the variation in the edge parameters is much more limited in this configuration. Therefore, the AUG results would also be consistent with DIII-D intrinsic edge rotation measurements in favorable drift configuration L-modes, for which only a weak dependence on n_e is observed.[97]

The dependence of v_ϕ on ν_i^* is interesting, because the currently most well-established theories on the generation of intrinsic edge rotation rather predict a dependence on T_i or ∇T_i only[98–100] and also measurements of intrinsic edge v_ϕ and $v_{\phi,\mathrm{imp}}$ in DIII-D show a similar dependence on the local T_i (or its gradient), for constant I_p, at least in the H-mode.[101] Therefore, it is also found that the intrinsic toroidal edge rotation is mostly co-current, which is in line with the present observations from AUG, because DIII-D usually operates at lower edge collisionalities than AUG. In the L-mode dataset presented here (with $|I_p| = 0.8$ MA), a pure dependence of v_ϕ on T_i (or its gradient) is not found, whereas the observed density dependence could be attributed to damping mechanisms of the parallel momentum due to atomic processes (charge exchange or ionization) with neutrals penetrating into the confined plasma. The importance of neutrals on the formation of the intrinsic edge rotation has been investigated experimentally together with simulations before, where in JET H-modes[20] and in AUG L-modes,[93] they have been found to play an important role, whereas at DIII-D, their impact on the intrinsic edge rotation was insignificant in H-mode pedestals.[102] The data set presented here, which concentrates on L-mode plasmas, could serve as a good basis for further investigations on the importance of the various mechanisms, which can influence the parallel momentum (residual stress, ion orbit losses, neutrals, SOL currents)[89] and, ultimately, E_r at the plasma edge.

Due to the linear dependence of E_r on v_ϕ [see also Eq. (3)], a correlation between $E_{r,\min}$ and the edge v_ϕ is observed [see Fig. 22(c)]. This causes that E_r in the confined region (represented by $E_{r,\min}$) decreases with increasing ν_i^*, as is shown in Fig. 22(b). However, also $E_{r,\max}$, the maximum of the SOL hill, decreases by about the same amount as $E_{r,\min}$. Although the positions of $E_{r,\min}$ and $E_{r,\max}$ can vary, which implies that the outer E_r gradient does not have to be constant over the entire observed collisionality range, the coherent change of edge and SOL E_r suggests a certain level of interaction between these two plasma regions. Recently, a similar behavior of the edge E_r with plasma density, as it is found at AUG, has been observed at JET in ion wave heated L-modes in favorable drift configuration.[103]

Also at Alcator C-Mod, a correlation between the intrinsic edge v_ϕ and parallel SOL flows was observed[1] and it was suggested that the parallel SOL flows set the boundary condition for the intrinsic toroidal edge rotation. Therefore, it was also found that the intrinsic edge v_ϕ at the OMP follows the direction of transport-driven SOL flows of the HFS. This leads to a co-current intrinsic edge v_ϕ in favorable and to a countercurrent intrinsic edge v_ϕ in the unfavorable drift configuration, which was confirmed experimentally. Thus, $v_{\phi,i}B_\theta$ could, dependent on the exact v_ϕ profile, potentially decrease $E_{r,\min}$ and lead to stronger edge E_r gradients in favorable and to an increase in $E_{r,\min}$ and weaker E_r gradients in unfavorable drift configuration, although no direct E_r measurements were available for these plasmas. It was concluded that this different behavior of the intrinsic toroidal edge rotation could explain the increased P_{LH} in unfavorable compared to the favorable drift configuration.[1]

At AUG, the behavior of the intrinsic toroidal edge rotation is different and v_ϕ is found to be co-current in all observed drift

configurations for a wide range of ν_i^* (the banana-plateau regime), in agreement with observations at DIII-D, although there differences in the intrinsic $|v_\phi|$ are found between favorable and unfavorable drift configurations.[104] A co-current v_ϕ adds always positively to E_r in either drift configuration, and, therefore, at AUG, it cannot explain the altered P_{LH} in the same way as suggested for Alcator C-Mod.

The intrinsic edge v_ϕ measurements at AUG show that the direction of v_ϕ changes with the sign and helicity of the magnetic field. This indicates that the corresponding parallel SOL flows are dominated by Pfirsch–Schlüter (PS) flows. This indirect assessment of the nature of the parallel SOL flows is in line with direct measurements of parallel SOL flows at TCV, JET, and DIII-D, where it was found that the field-dependent PS flows are the main component to the parallel SOL flows,[105,106] at least close to the separatrix.[104] Direct measurements of the parallel SOL flows in the different drift configurations in the L-mode and the investigation of their impact on quantities in the confined plasma are foreseen in the near future at AUG.

VIII. E_r AT THE CONFINEMENT TRANSITION

Three equilibrium E_r profiles, acquired in stable L-mode and I-mode phases 15 ms before the respective confinement transition (into I- or into H-mode), are shown in Fig. 23. The L-H transition in favorable drift configuration (violet) occurred with $P_{net} = 1.0$ MW. In the unfavorable drift configuration, the L-I transition (orange) was triggered with $P_{net} = 1.8$ MW and the I-H transition (dark red) with $P_{net} = 3.3$ MW. In order to have comparable plasma conditions, the presented E_r profiles are from three consecutive USN discharges (#37980, 37983, and 37985) in which the density was feedback-controlled to $4.5 \times 10^{19}\,m^{-3}$ and only the drift configuration as well as the amount of ECRH power was changed.

For each of the three E_r profiles (i.e., within one drift configuration), it is found that their inner and outer E_r gradients are, within the uncertainties, of comparable strength. This is connected to the fact that ECRH is used as a heating system in these plasmas, for which it is regularly observed that the outer E_r gradient is at least as steep as the inner E_r gradient. In NBI plasmas, the inner E_r gradient can be significantly stronger than the outer E_r gradient.

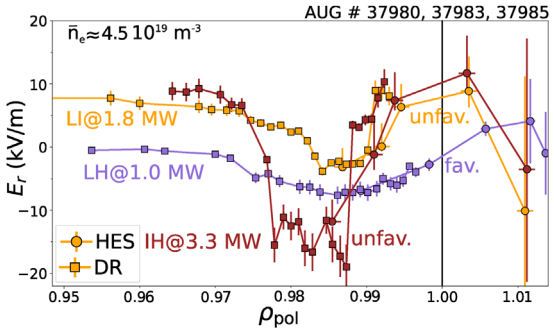

FIG. 23. Equilibrium E_r profiles at the confinement transition in favorable and unfavorable drift configuration plasmas of same density. Experimental edge E_r profiles acquired with DR (squares) and HES (circles) in the favorable drift configuration at the L-H transition (violet) and in the unfavorable drift configuration at the L-I transition (orange) and at the I-H transition (dark red). Figure adapted from Plank *et al.*, Plasma Phys. Controlled Fusion **65**, 014001 (2023). Copyright 2023 Author(s), licensed under a Creative Commons Attribution (CC BY) license.

A comparison of the E_r profiles among each other, i.e., between the different drift configurations, shows that they are all different. In favorable drift configuration, $E_{r,min}$ is at about −8 kV/m at the L-H transition, which is a relatively high value of $E_{r,min}$ compared to usually observed $E_{r,min}$ values in the favorable drift configuration at the L-H transition at AUG.[4,73] This $E_{r,min}$ value of −8 kV/m is in between the $E_{r,min}$ values of −3 kV/m found at the L-I transition and −12 kV/m at the I-H transition. The latter two are typical $E_{r,min}$ values observed in the unfavorable drift configuration at AUG at the confinement transitions into I- and H-modes, respectively.[75] In the SOL, the lowest $E_{r,max}$ is found for the favorable drift configuration, which is about 5 kV/m. The $E_{r,max}$ values in unfavorable drift configuration are at about 10 kV/m for both the L-mode and the I-mode phase. Compared to favorable drift configuration, the $E_{r,max}$ values are again located closer to the separatrix in the unfavorable drift configuration. Consequently, the weakest E_r gradients (inner and outer) are found at the L-H transition in the favorable drift configuration and the steepest gradients at the I-H transition in the unfavorable drift configuration. For these specific discharges, the E_r gradients at the L-I transition are comparable or slightly steeper than the E_r gradients at the L-H transition, but this is not a general feature. Plasmas of different parameters, e.g., at lower density, can also exhibit E_r gradients, which are weaker at the L-I transition than at the L-H transition.

These different E_r gradients observed at the respective confinement transitions show that there is not one a single critical E_r gradient at the confinement transition, which has to be reached in order to trigger the transition into H-mode (or I-mode), independent of the drift configuration. If it is the case that the mean $v_{E\times B}$ shear is responsible for the edge turbulence suppression, then the different E_r gradients may indicate that the strength or type of the characteristic turbulence is different in the different drift configurations. Indeed, turbulence in the I-mode, preceding an I-H transition, has different spectral features than typical L-mode plasma turbulence and it also gives lower thermal transport.[75,107–110] For this reason, it is foreseen to simulate these plasmas, employing experimental profiles and power fluxes, with gyrokinetic models in order to address the impact of the drift configuration on the edge turbulence and related quantities.

IX. SUMMARY AND CONCLUSIONS

In this experimental study at AUG, edge and SOL electron and ion kinetic profiles, rotation and E_r profiles were compared in L-modes of favorable and unfavorable drift configurations (in both LSN and USN plasmas with normal and reversed B_ϕ), using new and improved diagnostic capabilities. The improvement of these measurements and the systematic study of the behavior of these different quantities in the L-mode help to elucidate the mechanisms leading to the increased H-mode power threshold in unfavorable drift configuration. Special focus was put on the investigation of the equilibrium E_r across the separatrix and its characterization in the L-mode, right before the L-H transition.

It is found that the evolution of the equilibrium E_r during the L-H confinement transition is very similar between the two drift configurations. The E_r gradients steepen only significantly once an improved confinement regime has been entered, in agreement with observations at COMPASS-D[111] and JET.[112] It is found that in the transition from L- to H-mode, the E_r profile follows the evolution of $(\nabla_r p_i)/(en_i)$, but in the L-mode, strong deviations of E_r from $(\nabla_r p_i)/(en_i)$ are found in

both drift configurations, where $(\nabla_r p_i)/(en_i)$, $v_{\phi,i}B_\theta$, and $v_{\theta,i}B_\phi$ are similar in magnitude.

Comparisons of L-modes in different drift configurations with matched parameters (ECRH power and plasma density) show that the edge ion and electron profiles, including $(\nabla_r p_i)/(en_i)$, are the same, but the E_r well in the confined region is shallower in unfavorable compared to the favorable drift configuration. The maximum of E_r in the SOL is of comparable size in both drift configurations, which shows that the measured upstream SOL E_r is little influenced by the changed divertor conditions. However, the maximum of the SOL E_r is consistently found to be located closer to the separatrix in unfavorable compared to favorable drift configuration. Comparisons of the measured upstream E_r profiles to a simple 1D SOL model give good agreement in favorable drift configuration, but in unfavorable drift configuration, the E_r profiles are overestimated.

The experimental edge E_r profiles in the confined plasma are only in reasonable agreement with local NC theory. For the investigated L-mode plasmas, the strength of the measured inner E_r gradient is regularly underestimated by the NC predictions, particularly in favorable drift configuration. Also the differences found in the experimental E_r profiles between the two drift configurations cannot be reproduced by the local NC predictions. This indicates that other, non-neoclassical, effects are important to set E_r in the L-mode, which could produce a different edge E_r for the two drift configurations.

Comparisons of E_r profiles in favorable and unfavorable drift configuration and matched plasma density show that at the respective confinement transition (L-H, L-I, and I-H), the E_r gradients have a different strength. In the framework of a critical mean $E \times B$ shear needed to suppress turbulence, this could imply that the type or strength of the underlying edge turbulence is different for the different drift configurations. These differences will be assessed in the near future with the help of edge turbulence measurements and gyrokinetic simulations.[91] With the latter also the role of additional fluctuating shear flows, like zonal flows,[113] which are also often considered to be the responsible trigger for the L-H transition, but have not been scope of this work, can be addressed.

ECRH power and plasma density scans in the L-mode have shown that the intrinsic toroidal edge rotation and, with this, $E_{r,\min}$ in the confined plasma, order with edge collisionality, whereas the outer E_r gradient remains roughly constant in the L-mode, independent of the edge collisionality. Furthermore, the intrinsic toroidal edge rotation is found to be co-current in the banana-plateau regime and it becomes countercurrent when the PS-regime is reached. It is observed that in all investigated drift configurations, for a given collisionality, the intrinsic edge rotation is in the same direction (either co- or countercurrent), thus following the PS flows in the SOL. For this reason, the hypothesis of the increase in P_{LH} in unfavorable drift configuration due to countercurrent edge rotation impeding the L-H transition, as suggested by LaBombard *et al.* based on Alcator C-mod data,[1] cannot be confirmed in AUG.

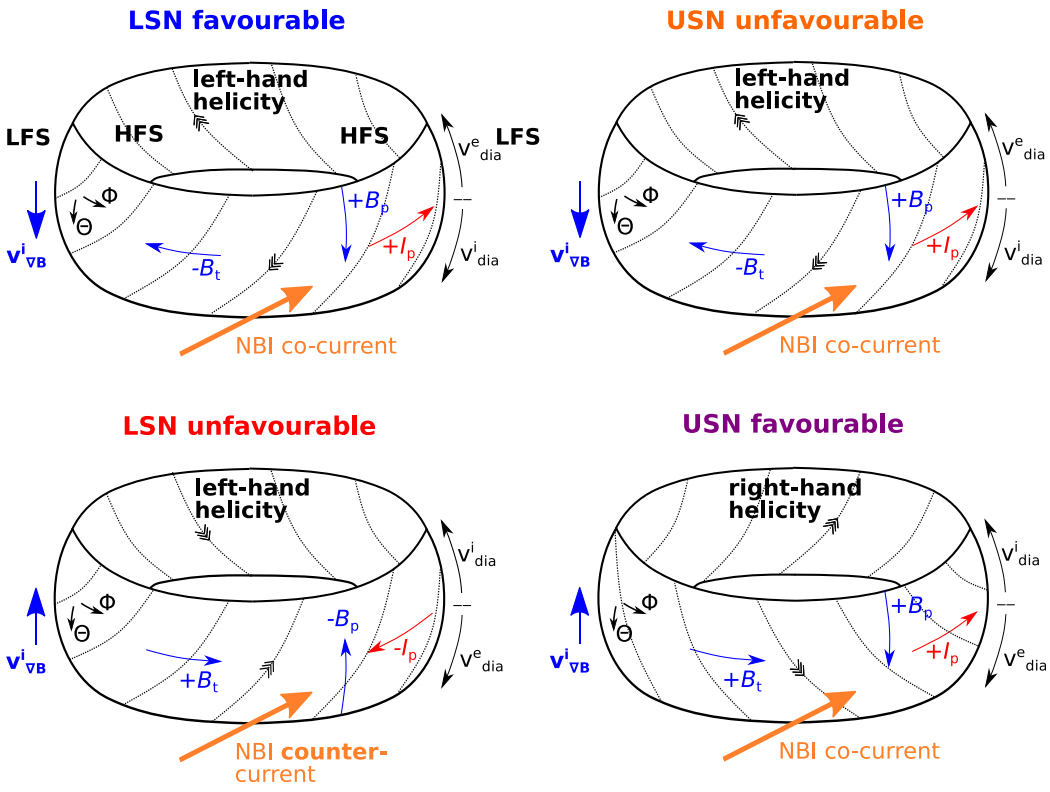

FIG. 24. Sign convention of AUG and the corresponding drift directions in the four investigated magnetic configurations at AUG.

In summary, it is found that the edge E_r is composed of a complex interaction between the main ion pressure gradient and the main ion flows, where the latter are found to be non-neoclassical. In specific circumstances, e.g., in low-density ECRH L-modes in unfavorable drift configuration, $(\nabla_r p_i)/(en_i)$ and $v_i \times B$ even have competing roles and, therefore, in these conditions an increase in the heating power does not necessarily lead to a steepening of the E_r gradients, but just to an upward shift of the entire edge E_r profile. The lack of dependence of the E_r gradients on heating power could also explain the increased H-mode threshold in such plasma conditions. Furthermore, these observations show that at least in the L-mode, it is not always valid to use the minimum of the edge E_r as a proxy for its gradients.

ACKNOWLEDGMENTS

The main author would like to thank Gregor Birkenmeier, Raul Gerrù-Miguelañez, Ondrej Grover, Rachael McDermott, Ulrich Stroth, and Elisabeth Wolfrum for fruitful discussions and valuable input.

This work has been carried out within the framework of the EUROfusion Consortium, funded by the European Union via the Euratom Research and Training Programme (Grant Agreement No. 101052200 – EUROfusion). Views and opinions expressed are, however, those of the author(s) only and do not necessarily reflect those of the European Union or the European Commission. Neither the European Union nor the European Commission can be held responsible for them.

The work of A. Hubbard was supported by U.S. Department of Energy Award Nos. DE-FC02-99ER54512 and DE-SC0014264.

AUTHOR DECLARATIONS

Conflict of Interest

The authors have no conflicts to disclose.

Author Contributions

Ulrike Plank: Conceptualization (lead); Data curation (lead); Formal analysis (lead); Investigation (lead); Methodology (lead); Software (equal); Validation (lead); Writing – original draft (lead); Writing – review & editing (lead). **Thomas Hubert Eich:** Formal analysis (supporting). **Rainer Fischer:** Formal analysis (supporting). **Pascale C. Hennequin:** Formal analysis (supporting); Writing – review & editing (supporting). **ASDEX Upgrade Team:** Conceptualization (supporting); Project administration (lead). **Dominik Brida:** Formal analysis (supporting); Investigation (supporting); Methodology (supporting). **Garrard Conway:** Formal analysis (supporting); Investigation (supporting); Methodology (supporting). **Tim Happel:** Formal analysis (supporting); Investigation (supporting); Methodology (supporting). **Amanda E. Hubbard:** Conceptualization (supporting); Resources (supporting); Writing – review & editing (supporting). **Thomas Pütterich:** Conceptualization (supporting); Investigation (supporting); Methodology (supporting); Supervision (lead). **Clemente Angioni:** Investigation (supporting); Validation (supporting); Writing – review & editing (supporting). **Marco Cavedon:** Conceptualization (supporting); Supervision (supporting). **Ralph Dux:** Software (equal); Validation (supporting).

DATA AVAILABILITY

The data that support the findings of this study are available from the corresponding author upon reasonable request.

APPENDIX A: COORDINATE SYSTEM AND MAGNETIC CONFIGURATIONS OF AUG

Figure 24 shows a bird's-eye view image, and Fig. 25 shows the poloidal cross sections of the different magnetic configurations (drift configurations) of AUG employed in this experimental study. AUG uses a right-handed, orthogonal (R, Θ, Φ) coordinate system (COCOS 17[114]) with Φ being counterclockwise if viewed from above and Θ pointing downward at the outer midplane (OMP). In the standard magnetic configuration, the lower-single null (LSN) favorable drift configuration (blue), B_ϕ is negative and directed clockwise if seen from above. In this configuration, I_p is counterclockwise and positive, which leads to a left-handed helicity of the magnetic field lines. The NBI injection is co-current.

Due to technical constraints, the helicity of the B-field has to be preserved in the lower divertor at AUG. Thus, the unfavorable drift configuration in LSN (red) can only be obtained if both B_ϕ and I_p are reversed, which leads to a countercurrent NBI injection. In the upper single-null (USN) unfavorable drift configuration (orange), the drift directions are the same as in the LSN favorable drift configuration, except that in this case, $v_{\nabla B,i}$ points away from the primary X-point. The USN favorable drift configuration can then simply be achieved by reversing B_ϕ only, which, at the same time, changes the helicity of the B-field to right-handed. The NBI injection is co-current in this case.

In Fig. 25, besides the directions of the ion ∇B-drift (blue), also the directions of the electron and ion diamagnetic drifts are indicated (black) at the high field side (HFS) and low field side (LFS). For the directions of the poloidal component of the $E \times B$ drift (shown in magenta), the following assumptions on E_r at the OMP were made: In the core plasma, E_r is dominated by the toroidal rotation and, thus, by the injection direction of the NBI and it is dominated by $(\nabla_r p_i)/(en_i)$ at the plasma edge. In the SOL, it was assumed to be positive.

APPENDIX B: SENSITIVITY STUDY OF THE NC PREDICTION OF E_r ON THE CHOICE OF THE T_i PROFILE

A sensitivity study has shown that the NC calculations of the main ion velocities and the resulting E_r profiles are most sensitive to the T_i input profiles. Therefore, in Fig. 26, a comparison of cubic-spline fits of different stiffness is shown, which were used to fit the edge T_i data in favorable [(a)—blue] and unfavorable [(b)—light red] drift configuration L-modes. These L-mode phases are also presented in Sec. VI A. The solid lines result from stiffer and the dashed lines from less stiff fits to the experimental T_i data. These different T_i fits were given as input to NEOART and the resulting E_r profiles are shown, together with the experimental data, in Fig. 27.

For producing the E_r profiles of both drift configurations, shown in Fig. 27(a), the stiffer fits were used (flat T_i gradient). For Fig. 27(b), less stiff fits were used, which allow for steeper gradients

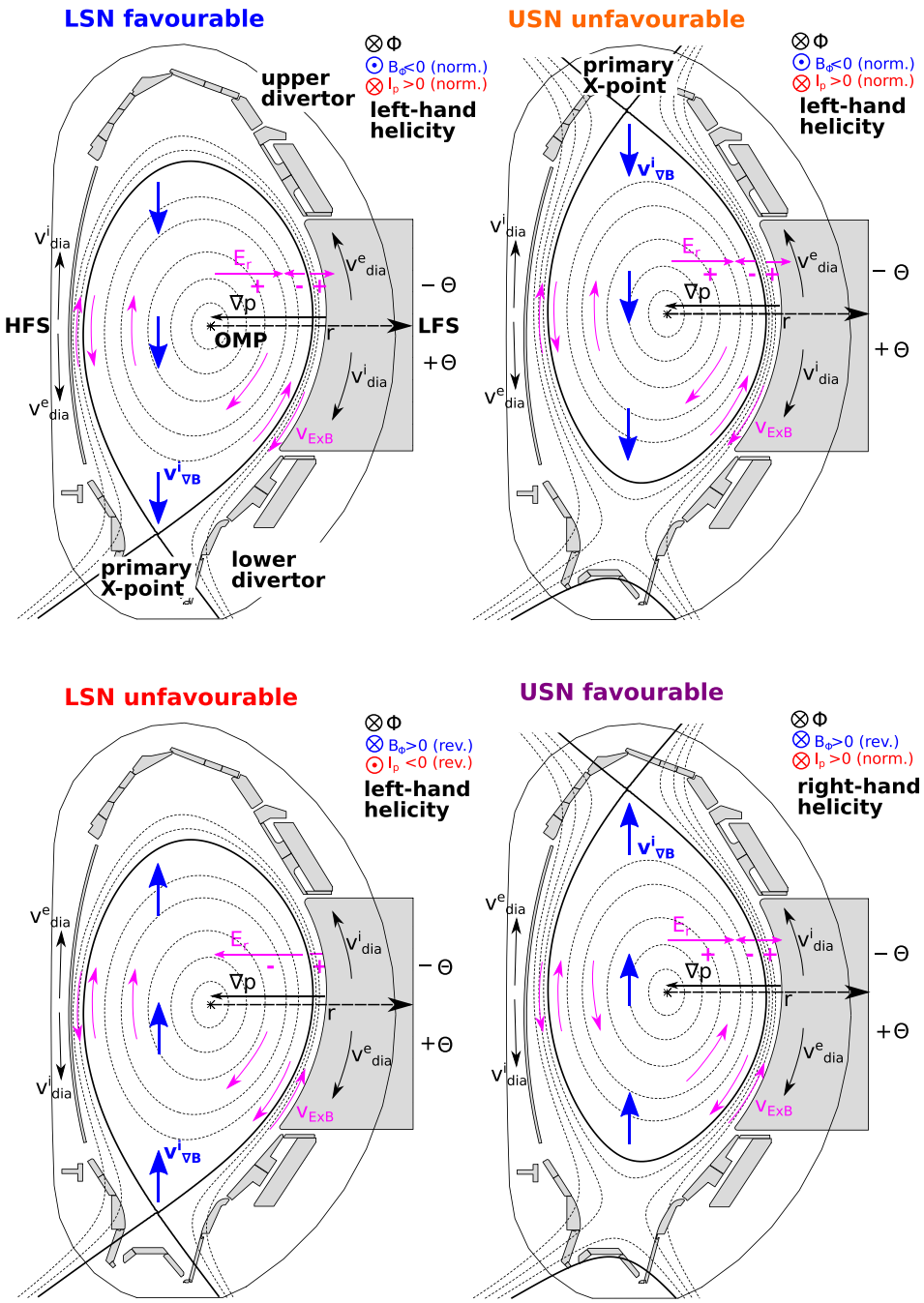

FIG. 25. Poloidal cross sections of the four investigated magnetic configurations at AUG. The directions of the different drifts are also indicated in the plots.

in the edge T_i profiles, but are at the same time more sensitive to outliers in the experimental T_i data. The figure shows that for the less stiff T_i fits the predicted E_r profiles agree qualitatively better with the measured E_r profiles in the region around $E_{r,\min}$ for the favorable drift configuration, whereas for the unfavorable drift configuration, larger differences are found. Also the minimum in the E_r profile can only be produced using the less stiff T_i fit; however, also with these fits, the slope of the inner E_r gradient cannot be fully reproduced. Furthermore, the differences observed in the experimental E_r between favorable and unfavorable drift configuration are not captured by the predicted E_r profiles, neither with the stiff nor the less stiff T_i profiles.

From this, it can be seen that conclusions on the different drift configurations can be drawn when comparing the experimental

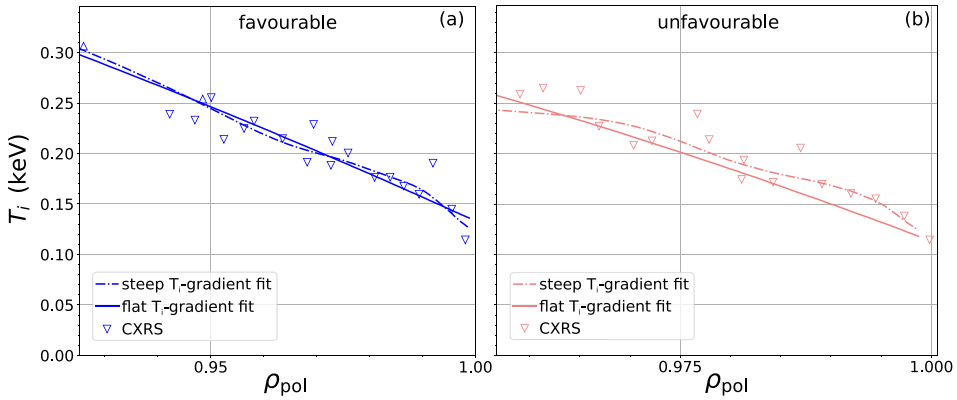

FIG. 26. T_i fits of different stiffness to the experimental edge T_i data of the L-mode phases presented in Sec. VI A. (a) Favorable and (b) unfavorable drift configurations.

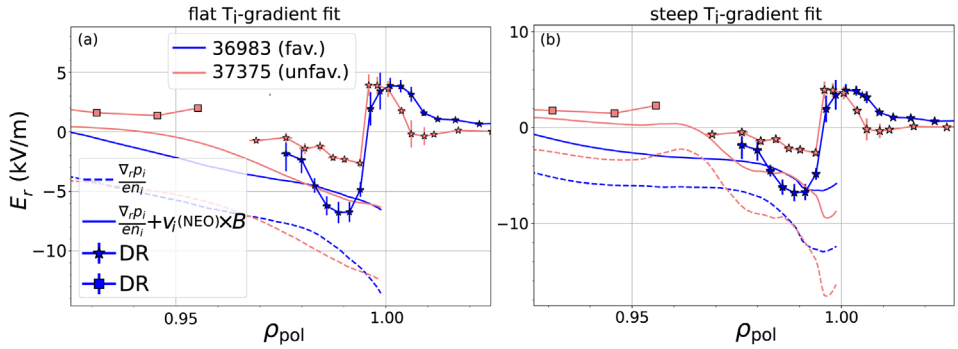

FIG. 27. Predicted E_r profiles from NEOART velocities (solid), main ion pressure gradient (dashed), and experimental edge E_r profiles (stars), using a stiff fit for the edge T_i data, allowing for less steep edge gradients (a), and using a less stiff fit for the edge T_i data, allowing for steeper edge gradients (b).

data with the NC predictions, independently of the exact shape of the input profiles, as long as fits of the same stiffness are used for the NC calculations.

REFERENCES

[1]B. LaBombard, J. E. Rice, A. E. Hubbard, J. W. Hughes, M. Greenwald, R. S. Granetz, J. H. Irby, Y. Lin, B. Lipschultz, E. S. Marmar, K. Marr, D. Mossessian, R. Parker, W. Rowan, N. Smick, J. A. Snipes, J. L. Terry, S. M. Wolfe, S. J. Wukitch, and Alcator C-Mod Team, Phys. Plasmas **12**, 056111 (2005).

[2]ASDEX Team, Nucl. Fusion **29**, 1959 (1989).

[3]H. Biglari, P. H. Diamond, and P. W. Terry, Phys. Fluids B **2**, 1 (1990).

[4]M. Cavedon, G. Birkenmeier, T. Pütterich, F. Ryter, E. Viezzer, E. Wolfrum, R. Dux, T. Happel, P. Hennequin, U. Plank, U. Stroth, M. Willensdorfer, and ASDEX Upgrade Team, Nucl. Fusion **60**, 066026 (2020).

[5]Y. R. Martin, T. Takizuka, and ITPA CDBM H-mode Threshold Database Working Group, J. Phys.: Conf. Ser. **123**, 012033 (2008).

[6]F. Ryter, W. Suttrop, B. Brüsehaber, M. Kaufmann, V. Mertens, H. Murmann, A. G. Peeters, J. Stober, J. Schweinzer, H. Zohm, and ASDEX Upgrade Team, Plasma Phys. Controlled Fusion **40**, 725 (1998).

[7]T. N. Carlstrom, K. H. Burrell, R. J. Groebner, and G. M. Staebler, "H-mode threshold power scaling and the ∇B drift effect," Report No. GA-A-22630; CONF-9706131-6 (General Atomics, San Diego, CA, 1997).

[8]M. Greenwald, R. L. Boivin, F. Bombarda, P. T. Bonoli, C. L. Fiore, D. Garnier, J. A. Goetz, S. N. Golovato, M. A. Graf, R. S. Granetz, S. Horne, A. Hubbard, I. H. Hutchinson, J. H. Irby, B. LaBombard, B. Lipschultz, E. S. Marmar, M. J. May, G. M. McCracken, P. OShea, J. E. Rice, J. Schachter, J. A. Snipes, P. C. Stek, Y. Takase, J. L. Terry, Y. Wang, R. Watterson, B. Welch, and S. M. Wolfe, Nucl. Fusion **37**, 793 (1997).

[9]D. G. Whyte, A. E. Hubbard, J. W. Hughes, B. Lipschultz, J. E. Rice, E. S. Marmar, M. Greenwald, I. Cziegler, A. Dominguez, T. Golfinopoulos, N. Howard, L. Lin, R. M. McDermottb, M. Porkolab, M. L. Reinke, J. Terry, N. Tsujii, S. Wolfe, S. Wukitch, Y. Lin, and Alcator C-Mod Team, Nucl. Fusion **50**, 105005 (2010).

[10]T. N. Carlstrom, R. J. Groebner, C. Fenzi, G. R. McKee, R. A. Moyer, and T. L. Rhodes, Plasma Phys. Controlled Fusion **44**, A333 (2002).

[11]J. Schirmer, G. D. Conway, H. Zohm, W. Suttrop, and ASDEX Upgrade Team, Nucl. Fusion **46**, S780 (2006).

[12]L. Vermare, P. Hennequin, C. Honoré, M. Peret, G. Dif-Pradalier, X. Garbet, J. Gunn, C. Bourdelle, F. Clairet, J. Morales, R. Dumont, M. Goniche, P. Maget, and R. Varennes, Nucl. Fusion **62**, 026002 (2022).

[13]L. Aho-Mantila, M. Wischmeier, H. W. Müller, S. Potzel, D. P. Coster, X. Bonnin, G. D. Conway, and ASDEX Upgrade Team, Nucl. Fusion **52**, 103006 (2012).

[14]A. V. Chankin, E. Delabie, G. Corrigan, D. Harting, C. F. Maggi, H. Meyer, and JET Contributors, Plasma Phys. Controlled Fusion **59**, 045012 (2017).

[15]P. Manz, T. Happel, U. Stroth, T. Eich, D. Silvagni, and ASDEX Upgrade Team, Nucl. Fusion **60**, 096011 (2020).

[16]N. Fedorczak, P. H. Diamond, G. Tynan, and P. Manz, Nucl. Fusion **52**, 103013 (2012).

[17]G. M. Staebler and R. J. Groebner, Plasma Phys. Controlled Fusion **57**, 014025 (2015).

[18]K. C. Shaing and E. C. Crume, Jr., Phys. Rev. Lett. **63**, 2369 (1989).

[19]R. W. Brzozowski, F. Jenko, R. Bilato, M. Cavedon, and ASDEX Upgrade Team, Phys. Plasmas **26**, 042511 (2019).

[20]T. W. Versloot, P. C. De Vries, C. Giroud, M. Brix, M. G. Von Hellermann, P. J. Lomas, D. Moulton, M. O. Mullane, I. M. Nunes, A. Salmi, T. Tala, I. Voitsekhovitch, K. D. Zastrow, and JET-EFDA Contributors, Plasma Phys. Controlled Fusion **53**, 065017 (2011).

[21]D. Moulton, G. Corrigan, J. R. Harrison, B. Lipschultz, and JET Contributors, Nucl. Fusion **58**, 096029 (2018).
[22]S. I. Braginskii, *Transport Processes in a Plasma* (Springer, New York, 1965), Chap. 3, p. 205.
[23]E. Viezzer, T. Pütterich, C. Angioni, A. Bergmann, R. Dux, E. Fable, R. M. McDermott, U. Stroth, E. Wolfrum, and ASDEX Upgrade Team, Nucl. Fusion **54**, 012003 (2014).
[24]S. R. Haskey, B. A. Grierson, C. Chrystal, A. Ashourvan, K. H. Burrell, R. J. Groebner, E. A. Belli, L. Stagner, D. J. Battaglia, T. Stoltzfus-Dueck, and A. Bortolon, Plasma Phys. Controlled Fusion **60**, 105001 (2018).
[25]R. J. Goldston and P. H. Rutherford, *Introduction to Plasma Physics* (IOP Publishing, Bristol and Philadelphia, 1995).
[26]P. C. Stangeby, *The Plasma Boundary of Magnetic Fusion Devices* (IOP Publishing, London, 2000).
[27]D. Brida, G. Conway, J. Adamek, D. Silvagni, P. David, T. Eich, G. Grenfell, M. Komm, U. Plank, and ASDEX Upgrade Team, Nucl. Mater. Energy **33**, 101262 (2022).
[28]A. V. Chankin, D. P. Coster, G. Corrigan, S. K. Erents, W. Fundamenski, A. Kallenbach, K. Lackner, J. Neuhauser, and R. Pitts, Plasma Phys. Controlled Fusion **51**, 065022 (2009).
[29]P. C. Stangeby and A. V. Chankin, Nucl. Fusion **36**, 839 (1996).
[30]M. Cavedon, R. Dux, T. Happel, P. Hennequin, U. Plank, T. Pütterich, F. Ryter, U. Stroth, E. Viezzer, E. Wolfrum, and ASDEX Upgrade Team, in 46th EPS Conference on Plasma Physics, 2019.
[31]U. Plank, T. Pütterich, C. Angioni, M. Cavedon, G. D. Conway, R. Fischer, T. Happel, A. Kappatou, R. M. McDermott, P. A. Schneider, G. Tardini, M. Weiland, and ASDEX Upgrade Team, Nucl. Fusion **60**, 074001 (2020).
[32]R. Fischer, C. J. Fuchs, B. Kurzan, W. Suttrop, E. Wolfrum, and ASDEX Upgrade Team, Fusion Sci. Technol. **58**, 675 (2010).
[33]F. Ryter, M. Cavedon, T. Happel, R. M. McDermott, E. Viezzer, G. D. Conway, R. Fischer, B. Kurzan, T. Pütterich, G. Tardini, M. Willensdorfer, and ASDEX Upgrade Team, Plasma Phys. Controlled Fusion **58**, 014007 (2016).
[34]R. M. McDermott, R. Dux, T. Pütterich, B. Geiger, A. Kappatou, A. Lebschy, C. Bruhn, M. Cavedon, A. Frank, N. D. Harder, E. Viezzer, and ASDEX Upgrade Team, Plasma Phys. Controlled Fusion **60**, 095007 (2018).
[35]R. Fischer, S. K. Rathgeber, S. Fietz, J. Hobirk, A. Kallenbach, H. Meister, T. Pütterich, F. Ryter, G. Tardini, E. Wolfrum, H. Zohm, and ASDEX Upgrade Team, in 37th EPS Conference on Plasma Physics, 2010.
[36]U. Plank, "The effect of the radial electric field around the separatrix on the access to the high confinement mode at ASDEX Upgrade," Ph.D. thesis (Ludwig Maximilian University Munich, 2021).
[37]G. D. Conway, C. Angioni, F. Ryter, P. Sauter, J. Vicente, and ASDEX Upgrade Team, Phys. Rev. Lett. **106**, 065001 (2011).
[38]H. Zohm, ASDEX Upgrade Team, and NI and ICRH Group, Phys. Rev. Lett. **72**, 222 (1994).
[39]H. Zohm, W. Suttrop, K. Buchl, H. J. De Blank, O. Gruber, A. Kallenbach, V. Mertens, F. Ryter, and M. Schittenhelm, Plasma Phys. Controlled Fusion **37**, 437 (1995).
[40]L. Schmitz, L. Zeng, T. L. Rhodes, J. C. Hillesheim, E. J. Doyle, R. J. Groebner, W. A. Peebles, K. H. Burrell, and G. Wang, Phys. Rev. Lett. **108**, 155002 (2012).
[41]O. Grover, J. Seidl, D. Refy, J. Adamek, P. Vondracek, M. Tomes, P. Junek, P. Hacek, J. Krbec, V. Weinzettl, M. Hron, S. Zoletnik, and COMPASS Team, Nucl. Fusion **58**, 112010 (2018).
[42]L. M. Shao, G. S. Xu, R. Chen, L. Chen, G. Birkenmeier, Y. M. Duan, W. Gao, P. Manz, T. H. Shi, H. Q. Wang, L. Wang, M. Xu, N. Yan, L. Zhang, and EAST Team, Plasma Phys. Controlled Fusion **60**, 035012 (2018).
[43]G. Birkenmeier, M. Cavedon, G. D. Conway, P. Manz, U. Stroth, R. Fischer, G. Fuchert, T. Happel, F. M. Laggner, M. Maraschek, A. Medvedeva, V. Nikolaeva, D. Prisiazhniuk, T. Pütterich, F. Ryter, L. M. Shao, M. Willensdorfer, E. Wolfrum, H. Zohm, and ASDEX Upgrade Team, Nucl. Fusion **56**, 086009 (2016).
[44]A. E. Hubbard, D. G. Whyte, R. M. Churchill, I. Cziegler, A. Dominguez, T. Golfinopoulos, J. W. Hughes, J. E. Rice, I. Bespamyatnov, M. J. Greenwald, N. Howard, B. Lipschultz, E. S. Marmar, M. L. Reinke, W. L. Rowan, J. L. Terry, and Alcator C-Mod Group, Phys. Plasmas **18**, 056115 (2011).
[45]T. Happel, P. Manz, D. Prisiazhniuk, F. Ryter, D. Silvagni, the D. Brida, M. Dunne, T. Eich, M. Faitsch, M. Griener, D. Nille, J. R. Pinzón, B. Sieglin, U. Stroth, H. J. Sun, S. J. Freethy, P. Hennequin, L. Gil, L. Guimarais, A. Merle, E. Viezzer, ASDEX Upgrade Team, and EUROfusion MST1 Team, in 27th IAEA Fusion Energy Conference, 2018.
[46]T. Happel, M. Griener, D. Silvagni, S. J. Freethy, P. Hennequin, F. Janky, P. Manz, D. Prisiazhniuk, F. Ryter, M. Bernert, D. Brida, T. Eich, M. Faitsch, L. Gil, L. Guimarais, A. Merle, D. Nille, J. Pinzón, B. Sieglin, U. Stroth, E. Viezzer, ASDEX Upgrade Team, and EUROfusion MST1 Team, Nucl. Mater. Energy **18**, 159 (2019).
[47]D. Silvagni, T. Eich, T. Happel, G. F. Harrer, M. Griener, M. Dunne, M. Cavedon, M. Faitsch, L. Gil, D. Nille, B. Tal, R. Fischer, U. Stroth, D. Brida, P. David, P. Manz, E. Viezzer, ASDEX Upgrade Team, and EUROfusion MST1 Team, Nucl. Fusion **60**, 126028 (2020).
[48]F. Ryter, L. Barrera Orte, B. Kurzan, R. M. McDermott, G. Tardini, E. Viezzer, M. Bernert, R. Fischer, and ASDEX Upgrade Team, Nucl. Fusion **54**, 083003 (2014).
[49]M. Weiland, R. Bilato, R. Dux, B. Geiger, A. Lebschy, F. Felici, R. Fischer, D. Rittich, M. Van Zeeland, ASDEX Upgrade Team, and EUROfusion MST1 Team, Nucl. Fusion **58**, 082032 (2018).
[50]P. David, M. Bernert, T. Pütterich, C. Fuchs, S. Glöggler, T. Eich, and ASDEX Upgrade Team, Nucl. Fusion **61**, 066025 (2021).
[51]G. V. Pereverzev and P. N. Yushmanov, "ASTRA-Automated System for Transport Analysis in a Tokamak," Report No. IPP 5/98 (Max Planck Institute for Plasma Physics, 2002).
[52]E. Poli, A. G. Peeters, and G. V. Pereverzev, Comput. Phys. Commun. **136**, 90 (2001).
[53]R. Fischer, A. Bock, A. Burckhart, M. Dunne, O. Ford, J. C. Fuchs, L. Giannone, A. Gude, V. Igochine, A. Lebschy, M. Maraschek, P. J. McCarthy, A. Mlynek, A. Snicker, J. Stober, G. Tardini, M. Weiland, M. Willensdorfer, and ASDEX Upgrade Team, in 43rd EPS Conference on Plasma Physics, 2016.
[54]J. Illerhaus, "Estimation, validation and uncertainty of the position of the separatrix contour at ASDEX Upgrade," Diploma thesis (Technical University Munich, 2018).
[55]H. J. Sun, E. Wolfrum, T. Eich, B. Kurzan, S. Potzel, U. Stroth, and ASDEX Upgrade Team, Plasma Phys. Controlled Fusion **57**, 125011 (2015).
[56]T. Eich, P. Manz, R. J. Goldston, P. Hennequin, P. David, M. Faitsch, B. Kurzan, B. Sieglin, E. Wolfrum, ASDEX Upgrade Team, and EUROfusion MST1 Team, Nucl. Fusion **60**, 056016 (2020).
[57]D. Silvagni, T. Eich, M. Faitsch, T. Happel, B. Sieglin, P. David, D. Nille, L. Gil, U. Stroth, ASDEX Upgrade Team, and EUROfusion MST1 Team, Plasma Phys. Controlled Fusion **62**, 045015 (2020).
[58]M. Griener, J. M. Burgos, M. Cavedon, G. Birkenmeier, R. Dux, B. Kurzan, O. Schmitz, B. Sieglin, U. Stroth, E. Viezzer, E. Wolfrum, and ASDEX Upgrade Team, Plasma Phys. Controlled Fusion **60**, 025008 (2018).
[59]R. M. McDermott, A. Lebschy, B. Geiger, C. Bruhn, M. Cavedon, M. Dunne, R. Dux, R. Fischer, A. Kappatou, T. Pütterich, E. Viezzer, and ASDEX Upgrade Team, Rev. Sci. Instrum. **88**, 073508 (2017).
[60]E. Viezzer, T. Pütterich, R. Dux, and R. M. McDermott, Rev. Sci. Instrum. **83**, 103501 (2012).
[61]E. Viezzer, T. Pütterich, G. D. Conway, R. Dux, T. Happel, J. C. Fuchs, R. M. McDermott, F. Ryter, B. Sieglin, W. Suttrop, M. Willensdorfer, E. Wolfrum, and ASDEX Upgrade Team, Nucl. Fusion **53**, 053005 (2013).
[62]G. D. Conway, J. Schirmer, S. Klenge, W. Suttrop, E. Holzhauer, and ASDEX Upgrade Team, Plasma Phys. Controlled Fusion **46**, 951 (2004).
[63]T. Happel, A. B. Navarro, G. D. Conway, C. Angioni, M. Bernert, M. Dunne, E. Fable, B. Geiger, T. Görler, F. Jenko, R. M. McDermott, F. Ryter, U. Stroth, and ASDEX Upgrade Team, Phys. Plasmas **22**, 032503 (2015).
[64]H. Meyer, C. Bunting, G. Carolan, J. Conway, R. Dunstan, A. Kirk, R. Scannell, D. Temple, M. Walsh, and MAST and NBI Teams, J. Phys. Conf. Ser. **123**, 012005 (2008).
[65]A. G. Peeters, Phys. Plasmas **7**, 268 (2000).
[66]E. A. Belli and J. Candy, Plasma Phys. Controlled Fusion **50**, 095010 (2008).
[67]R. Dux, "STRAHL User Manual," Report No. IPP 10/30 (Max Planck Institute for Plasma Physics, 2006).

[68]F. Ryter, S. K. Rathgeber, L. Barrera Orte, M. Bernert, G. D. Conway, R. Fischer, T. Happel, B. Kurzan, R. M. McDermott, A. Scarabosio, W. Suttrop, E. Viezzer, M. Willensdorfer, E. Wolfrum, and ASDEX Upgrade Team, Nucl. Fusion **53**, 113003 (2013).
[69]F. Ryter, R. Fischer, J. C. Fuchs, T. Happel, R. M. McDermott, E. Viezzer, E. Wolfrum, L. Barrera Orte, M. Bernert, A. Burckhart, S. Da Graça, B. Kurzan, P. McCarthy, T. Pütterich, W. Suttrop, M. Willensdorfer, and ASDEX Upgrade Team, Nucl. Fusion **57**, 016004 (2017).
[70]T. N. Carlstrom, P. Gohil, J. G. Watkins, K. H. Burrell, S. Coda, E. J. Doyle, R. J. Groebner, J. Kim, R. A. Moyer, and C. L. Rettig, Plasma Phys. Controlled Fusion **36**, A147 (1994).
[71]P. Gohil, T. C. Jernigan, T. H. Osborne, J. T. Scoville, and E. J. Strait, Nucl. Fusion **50**, 064011 (2010).
[72]N. Bonanomi, C. Angioni, U. Plank, P. A. Schneider, C. F. Maggi, ASDEX Upgrade Team, EUROFusion MST1 Team, and JET Contributors, Phys. Plasmas **28**, 052504 (2021).
[73]P. Sauter, T. Pütterich, F. Ryter, E. Viezzer, E. Wolfrum, G. D. Conway, R. Fischer, B. Kurzan, R. M. McDermott, S. K. Rathgeber, and ASDEX Upgrade Team, Nucl. Fusion **52**, 012001 (2012).
[74]M. Cavedon, T. Pütterich, E. Viezzer, G. Birkenmeier, T. Happel, F. M. Laggner, P. Manz, F. Ryter, U. Stroth, and ASDEX Upgrade Team, Nucl. Fusion **57**, 014002 (2017).
[75]T. Happel, P. Manz, F. Ryter, M. Bernert, M. Dunne, P. Hennequin, A. Hetzenecker, U. Stroth, G. D. Conway, L. Guimarais, C. Honoré, E. Viezzer, and ASDEX Upgrade Team, Plasma Phys. Controlled Fusion **59**, 014004 (2017).
[76]H. Meyer, P. G. Carolan, G. D. Conway, G. Cunningham, L. D. Horton, A. Kirk, R. Maingi, F. Ryter, S. Saarelma, J. Schirmer, W. Suttrop, H. R. Wilson, MAST, ASDEX Upgrade, and NSTX Teams, Nucl. Fusion **46**, 64 (2006).
[77]J. Boedo, D. Gray, G. Tynan, R. Pitts, K. Dippel, K. Finken, and R. Conn, J. Nucl. Mater. **196–198**, 489 (1992).
[78]A. V. Chankin, J. Nucl. Mater. **241–243**, 199 (1997).
[79]T. Rognlien, G. Porter, and D. Ryutov, J. Nucl. Mater. **266–269**, 654 (1999).
[80]A. V. Chankin, G. Corrigan, M. Groth, P. C. Stangeby, and JET Contributors, Plasma Phys. Controlled Fusion **57**, 095002 (2015).
[81]I. Paradela Pérez, M. Groth, M. Wischmeier, A. Scarabosio, D. Brida, P. David, D. Silvagni, D. Coster, T. Lunt, M. Faitsch, ASDEX Upgrade Team, and EUROfusion MST1 Team, Nucl. Mater. Energy **19**, 531 (2019).
[82]J. A. Boedo, M. J. Schaffer, R. Maingi, and C. J. Lasnier, Phys. Plasmas **7**, 1075 (2000).
[83]T. Eich, A. W. Leonard, R. A. Pitts, W. Fundamenski, R. J. Goldston, T. K. Gray, A. Herrmann, A. Kirk, A. Kallenbach, O. Kardaun, A. S. Kukushkin, B. Labombard, R. Maingi, M. A. Makowski, A. Scarabosio, B. Sieglin, J. Terry, A. Thornton, and ASDEX Upgrade Team, Nucl. Fusion **53**, 093031 (2013).
[84]R. A. Moyer, K. H. Burrell, T. N. Carlstrom, S. Coda, R. W. Conn, E. J. Doyle, P. Gohil, R. J. Groebner, J. Kim, R. Lehmer, W. A. Peebles, M. Porkolab, C. L. Rettig, T. L. Rhodes, R. P. Seraydarian, R. Stockdale, D. M. Thomas, G. R. Tynan, and J. G. Watkins, Phys. Plasmas **2**, 2397 (1995).
[85]G. McKee, P. Gohil, D. Schlossberg, J. Boedo, K. Burrell, J. deGrassie, R. Groebner, R. Moyer, C. Petty, T. Rhodes, L. Schmitz, M. Shafer, W. Solomon, M. Umansky, G. Wang, A. White, and X. Xu, Nucl. Fusion **49**, 115016 (2009).
[86]N. Fedorczak, P. Ghendrih, P. Hennequin, G. R. Tynan, P. H. Diamond, and P. Manz, Plasma Phys. Controlled Fusion **55**, 124024 (2013).
[87]P. Manz, A. Stegmeir, B. Schmid, T. T. Ribeiro, G. Birkenmeier, N. Fedorczak, S. Garland, K. Hallatschek, M. Ramisch, and B. D. Scott, Phys. Plasmas **25**, 072508 (2018).
[88]G. M. Staebler and R. J. Groebner, Nucl. Fusion **55**, 73008 (2015).
[89]T. Stoltzfus-Dueck, Plasma Phys. Controlled Fusion **61**, 124003 (2019).
[90]J. Omotani, I. Pusztai, S. Newton, and T. Fülöp, Nucl. Fusion **56**, 124002 (2016).
[91]W. Zholobenko, A. Stegmeir, M. Griener, G. D. Conway, T. Body, D. Coster, F. Jenko, and ASDEX Upgrade Team, Nucl. Fusion **61**, 116015 (2021).
[92]P. Cano-Megias, E. Viezzer, R. Brzozowski, A. Jansen van Vuuren, D. J. Cruz-Zabala, M. Cavedon, R. Chacartegui, R. Dux, M. Garcia-Munoz, U. Plank, and ASDEX Upgrade Team, in 47th EPS Conference on Plasma Physics, 2021.
[93]J. T. Omotani, S. L. Newton, I. Pusztai, E. Viezzer, T. Fülöp, and ASDEX Upgrade Team, Nucl. Fusion **57**, 066048 (2017).
[94]S. Buller, I. Pusztai, S. L. Newton, and J. T. Omotani, Plasma Phys. Controlled Fusion **59**, 055019 (2017).
[95]R. Schneider, X. Bonnin, K. Borrass, D. P. Coster, H. Kastelewicz, D. Reiter, V. A. Rozhansky, and B. J. Braams, Contrib. Plasma Phys. **46**, 3–191 (2006).
[96]B. P. Duval, A. Bortolon, A. Karpushov, R. A. Pitts, A. Pochelon, O. Sauter, A. Scarabosio, G. Turri, and TCV Team, Phys. Plasmas **15**, 056113 (2008).
[97]A. Ashourvan, B. A. Grierson, D. J. Battaglia, S. R. Haskey, and T. Stoltzfus-Dueck, Phys. Plasmas **25**, 056114 (2018).
[98]T. Stoltzfus-Dueck, Phys. Rev. Lett. **108**, 065002 (2012).
[99]T. Stoltzfus-Dueck, Phys. Plasmas **19**, 055908 (2012).
[100]Y. Kosuga, P. H. Diamond, and Ö. D. Gürcan, Phys. Plasmas **17**, 102313 (2010).
[101]J. S. deGrassie, R. J. Groebner, K. H. Burrell, and W. M. Solomon, Nucl. Fusion **49**, 085020 (2009).
[102]C. Chrystal, B. A. Grierson, S. R. Haskey, A. C. Sontag, F. M. Poli, M. W. Shafer, and J. S. deGrassie, Nucl. Fusion **60**, 036003 (2020).
[103]C. Silva, E. R. Solano, J. C. Hillesheim, E. Delabie, S. Aleiferis, G. Birkenmeier, L. Gil, C. Giroud, E. Litherland-Smith, R. B. Morales, D. Nina, A. Silva, and JET Contributors, Nucl. Fusion **61**, 126006 (2021).
[104]J. A. Boedo, J. S. deGrassie, B. Grierson, T. Stoltzfus-Dueck, D. J. Battaglia, D. L. Rudakov, E. A. Belli, R. J. Groebner, E. Hollmann, C. Lasnier, W. M. Solomon, E. A. Unterberg, J. Watkins, and DIII-D Team, Phys. Plasmas **23**, 092506 (2016).
[105]R. A. Pitts, J. Horacek, and TCV Team, "Neoclassical and transport driven parallel SOL flows on TCV," in 34th EPS Conference on Plasma Physics, 2007.
[106]S. K. Erents, A. V. Chankin, G. F. Matthews, and P. C. Stangeby, Plasma Phys. Controlled Fusion **42**, 905 (2000).
[107]T. Happel, P. Manz, F. Ryter, P. Hennequin, A. Hetzenecker, G. D. Conway, L. Guimarais, C. Honoré, U. Stroth, E. Viezzer, and ASDEX Upgrade Team, Nucl. Fusion **56**, 064004 (2016).
[108]P. Manz, T. Happel, F. Ryter, M. Bernert, G. Birkenmeier, G. D. Conway, M. Dunne, L. Guimarais, P. Hennequin, A. Hetzenecker, C. Honoré, P. Lauber, M. Maraschek, V. E. Nikolaeva, D. Prisiazhniuk, U. Stroth, E. Viezzer, and ASDEX Upgrade Team, Nucl. Fusion **57**, 086022 (2017).
[109]A. E. White, P. Phillips, D. G. Whyte, A. E. Hubbard, C. Sung, J. W. Hughes, A. Dominguez, J. Terry, and I. Cziegler, Nucl. Fusion **51**, 113005 (2011).
[110]I. Cziegler, P. H. Diamond, N. Fedorczak, P. Manz, G. R. Tynan, M. Xu, R. M. Churchill, A. E. Hubbard, B. Lipschultz, J. M. Sierchio, J. L. Terry, and C. Theiler, Phys. Plasmas **20**, 055904 (2013).
[111]H. Meyer, P. G. Carolan, N. J. Conway, A. R. Field, S. J. Fielding, and P. Helander, Czechoslov. J. Phys. **50**, 1451 (2000).
[112]C. Silva, E. Solano, J. Hillesheim, E. Delabie, G. Birkenmeier, L. Gil, C. Giroud, R. Morales, D. Nina, and JET Contributors, Nucl. Fusion **62**, 126057 (2022).
[113]P. H. Diamond, S. I. Itoh, K. Itoh, and T. S. Hahm, Plasma Phys. Controlled Fusion **47**, R35 (2005).
[114]O. Sauter and S. Y. Medvedev, Comput. Phys. Commun. **184**, 293 (2013).